

Performance optimization of a subsonic Diffuser-Collector subsystem using interchangeable geometries

Brian P. Boehm

Thesis submitted to the faculty of the Virginia Polytechnic Institute and State University in partial fulfillment of the requirements for the degree of

**Master of Science
in
Mechanical Engineering**

Dr. K. Todd Lowe, Chair
Dr. Wing F. Ng
Dr. Clint L. Dancey

November 30th, 2012
Blacksburg, VA

Keywords: Diffuser-Collector Subsystem, Gas Turbine Exhaust Collector, Exhaust Collector Box, Tilted Diffuser, Secondary Flow, Radial Diffuser, Cutback Radial Diffuser

Performance optimization of a subsonic Diffuser-Collector subsystem using interchangeable geometries

Brian P. Boehm

ABSTRACT

A subsonic wind tunnel facility was designed and built to test and optimize various diffuser-collector box geometries at the one-twelfth scale. The facility was designed to run continuously at an inlet Mach number of 0.42 and an inlet hydraulic diameter Reynolds number of 340,000. Different combinations of diffusers, hubs, and exhaust collector boxes were designed and evaluated for overall optimum performance. Both 3-hole and 5-hole probes were traversed into the flow to generate multiple diffuser inlet and collector exit performance profile plots. Surface oil flow visualization was performed to gain an understanding of the complex 3D flow structures inside the diffuser-collector subsystem. The cutback radial hardware was found to increase the subsystem pressure recovery by over 10% from baseline resulting in an approximate 1% increase in gas turbine power output.

ACKNOWLEDGEMENTS:

The research presented in this thesis was made possible by several different people. First, I would like to thank the sponsors at Solar Turbines, Inc., Ulrich Stang and Hans Hamm Jr. for giving me the opportunity to pursue an exciting project and strengthen my professional experience. Their continued support and great depth of knowledge provided me with a detailed understanding of real world application in the gas turbine power generation field of study.

Next, I want to thank the team at Techsburg, Inc., Stephen Guillot, Nihar Samal (now at Solar Turbines), Jon Fleming, and Matt Langford for their mentorship and continuous support throughout the entire project. Their vast experimental research knowledge provided me with any on-site aid when needed and strengthened my experimental research capabilities. The fun working while learning environment couldn't have been possible without these guys.

Finally, I would like to thank the members of my committee Drs. Lowe, Ng, and Dancey who stood beside me throughout my graduate studies strengthening my education each and every day. I greatly appreciate the hospitality from Dr. Ng's company, Techsburg, Inc., providing me with a one of a kind learning environment. The important feedback I received from Dr. Dancey strengthened my problem solving skills and I thank him for his lasting contributions. A special thanks goes out to my chair committee member Dr. Lowe for his excellent mentorship, continuous encouragement, and countless one-on-one meetings making this research project truly the best.

TABLE OF CONTENTS:

ACKNOWLEDGEMENTS: iii

TABLE OF CONTENTS: iv

INDEX OF FIGURES: vi

INDEX OF TABLES: ix

INDEX OF EQUATIONS: x

NOMENCLATURE: x

 Acronyms x

 Greek xi

 Variables xi

 Subscripts xii

 Accents xii

Chapter 1 - INTRODUCTION 1

 1.1: Background of a Gas Turbine Diffuser 1

 1.1.1: Previous Diffuser Research 2

 1.2: Background of a Diffuser-Collector Exhaust Box 3

 1.2.1: Previous Diffuser-Collector Research 3

 1.2.2: Diffuser-Collector Subsystem Patents 4

 1.3: Fundamental Fluid Flow in 90 Degree Bends and of Impinging Jets 5

Chapter 2 - Small Scale Diffuser-Collector Research Facility Purpose and Design 7

 2.1: Busch Panther Continuous Blower 7

 2.2: Wind Tunnel Ductwork 8

 2.2.1: Pipe Flow Path and Material 8

 2.2.2: Pipe Flow Conditioner 9

 2.3: Design and Configuration of the Inlet Flow Conditioning Components 10

 2.3.1: Large Contraction Flange 10

 2.3.2: Turbulence Grid 11

 2.3.3: Swirl Vanes 12

 2.3.4: Boundary Layer Contraction 13

2.3.5: Struts.....	13
Chapter 3 - Instrumentation, Data Acquisition, and Processing	14
3.1: Data Acquisition Software & Temperature/Pressure Hardware	14
3.2: Diffuser Inlet Measurements	15
3.3: Collector Exit Section Measurements	17
3.4: Uncertainty Analysis.....	18
Chapter 4 - Baseline Diffuser-Collector Scaled Design, Results, and Discussion	20
4.1: Experimental Baseline Diffuser-Collector Box Design and Components.....	20
4.1.1: Baseline Back-Wall and Hub	21
4.2 Baseline Geometry Results and Discussion.....	22
4.2.1: Diffuser Inlet Conditions and Overall Subsystem Performance.....	23
4.2.2 Collector Exit Section Data	27
4.2.3 Oil Flow Visualization.....	28
Chapter 5 - Interchangeable Geometry Designs, Results, & Discussion	30
5.1: Flat Wall Collector Box Analysis	30
5.1.1: Diffuser Inlet Parameters and Overall Subsystem Performance	31
5.1.2: Collector Exit Section Data	33
5.2: Tilted Diffuser-Flat Wall Collector Analysis	34
5.2.1: Diffuser Inlet Parameters and Overall Subsystem Performance	35
5.2.2: Collector Exit Section Data	39
5.3: Radial Diffuser-Pinch Collector Analysis	41
5.3.1: Diffuser Inlet Parameters and Overall Subsystem Performance	42
5.3.2: Collector Exit Section Data	46
5.3.3 Oil Flow Visualization.....	48
5.4 Cutback Radial Diffuser-Flat Wall Collector Analysis	50
5.4.1: Diffuser Inlet Parameters and Overall Subsystem Performance	51
5.4.2: Collector Exit Section Data	53
5.4.3 Oil Flow Visualization.....	54
5.5: Diffuser Only Testing	56

Chapter 6 - Conclusion, Recommendations, and Future Work	58
6.1 Conclusion	58
6.2 Recommendations and Future Work	58
References	60
Appendix A - Other Experimentally Tested Geometries	62
Radial Hub Geometry and Results	62
Acura 60 Struts and Swirl Vanes	63
Appendix B - Additional Testing and Trends.....	64
Turning Strut Ring 180 Degrees	64
Calculation of Subsystem Pressure Recovery Based on a Trendline	65
Appendix C - All Experimentally Tested Diffuser-Collector Configurations.....	67

INDEX OF FIGURES:

Figure 1-1: Cut-Away View of the Fundamental Components of an Axial Flow Gas Turbine System. Solar Turbines Inc. Used with Written Permission.	1
Figure 1-2: Fundamental CFD Model of Fluid Flow Velocity within a 90 Degree Elbow	5
Figure 2-1: Busch Panther WA3125DP Continuous Blower with the Inlet and Outlet Locations Labeled.....	8
Figure 2-2: a) Individual PVC Schedule 80 Piping Components. b) Flow Path of the Assembled PVC Components Attached to the Blower Exhaust.	9
Figure 2-3: Pipe Flow Conditioner Placed Upstream of the Contraction Flange. The Four (4) Metal Discs Containing Mesh Screens are labeled.	9
Figure 2-4: Section View of the Flow Conditioning Components Upstream of the Diffuser-Collector.....	10
Figure 2-5: a) Contraction Flange Shown to Scale by a Quarter b) Contraction Flange Bolted to Upstream Pipe Flow Conditioner. The O-ring is Shown Installed in Both Pictures.	11
Figure 2-6: a) Turbulence Grid Bolted between the Nose Cone and Hub components. Shown to Scale by a Quarter. b) Upstream View through the Boundary Layer Contraction Section of the Perforated Turbulence Grid.....	12
Figure 2-7: Swirl Vane Ring Made From SLS Rapid Prototyping Shown to Scale by a Quarter. .	12
Figure 2-8: a) Zoomed in View Showing the Boundary Layer Contraction Colored in Green. b) Sub Assembly of the Boundary Layer Contraction Section Scaled by a Quarter.....	13

Figure 2-9: a) Section View of the Strut Ring (yellow) Assembled Having Equivalent Expansion Ratio as the Diffuser. b) Nylon SLS Strut Ring Scaled by a Quarter with O-rings Installed. ... 14

Figure 3-1: a) Labview Program used for Acquiring Time Averaged Data and Stepper Motor Traverse Control. b) Thermocouple Placed at the Exhaust of the Blower. c) Scanivalve Corp ZOC17 8-Channel Pressure Transducer. 14

Figure 3-2: a) An Upstream View of the Circumferential Radial Traverse Locations in Reference to the Pinch Collector Box. b) Experimental Setup of a Radial Traverse Using the 3-hole Wedge Probe at the 0° Location..... 16

Figure 3-3: a) Isometric View of the Exit Traverse Plane Shown in Green with the Back Wall and Hub Removed. b) Experimental Setup of the Exit Traverse Utilizing Two Stepper Motors and the 5-hole Probe. 17

Figure 4-1: a) Section View of the Solar Turbines Full Scale Production Model Geometry. b) Section View of Simplified Experimental One-Twelfth Scale Geometry. 20

Figure 4-2: a) Section View of the One-Twelfth Scale Baseline Diffuser-Collector Subsystem. b) Experimental SLS Baseline Pinch Collector Box. c) Baseline Aluminum Diffuser Scaled by a Quarter..... 21

Figure 4-3: a) Back wall of the Collector Box Made From Clear Acrylic Material b) Front View of the Baseline Hub Showing the Various Static Pressure Ports. 22

Figure 4-4: Circumferential Distribution of Inlet Total and Static Pressure Coefficients Along with Inlet Mach number. 24

Figure 4-5: a) Static Pressure Profile in the Diffuser of the Baseline Diffuser-Collector Configuration. The Theoretical Static Pressure of the Diffuser and Collector are shown for Reference. b) Inlet Circumferential Pressure Distribution at $x/L = 0$ for the Diffuser as well as at the Case and Hub. 25

Figure 4-6: a) Contour Plot of the Radial Velocity Out of the Page (U_y) Within the Exit Section of the Baseline Diffuser-Collector Geometry. b) Flow Magnitude and Direction Shown by a Vector Plot of the Baseline Diffuser-Collector Geometry. The Collector Exit Velocity is Normalized by the Diffuser Inlet Velocity (U_{ex}/U_{in}). 27

Figure 4-7: Surface Oil Flow Visualization in the Baseline Diffuser-Collector Configuration showing the Streamlines of the Diffuser and 180 Degree Portion of the Pinch Collector Box. 28

Figure 4-8: a) Streamlines on the Baseline Hub and Back wall. b) Close up of the Flow Reversal Streamlines on the Baseline Hub Between 0 to 90 Degrees. c) Separation Point on the Hub at the 180 Degree Location..... 29

Figure 5-1: a) Rear View of the Baseline Pinch ECB (left) and Flat Wall ECB (right). b) Side View of the Baseline Pinch ECB (left) and Flat Wall ECB (right). 30

Figure 5-2: a) Section View of the Baseline Diffuser-Collector Geometry. Section View of the Baseline Components with the Flat Wall ECB Substituted. Figures are shown Side by Side for Comparison.....	31
Figure 5-3: A Comparison of Baseline and Flat Wall Collector Geometry of the Circumferential Distribution of Inlet Total and Static Pressure Coefficients Along with Mach number.	32
Figure 5-4: A comparison of Exit Contour and Vector Plots Between the Baseline Diffuser-Collector Geometry (left) and the Substituted Flat Wall ECB Geometry (right). The Collector Exit Velocity is Normalized by the Diffuser Inlet Velocity.	33
Figure 5-5: a) Section View of the 9 Degree Tilted Diffuser with Flat Wall Collector. b) Experimental 9 Degree SLS Tilted Diffuser Shown to Scale by a Quarter.	34
Figure 5-6: Tilted Diffuser Analysis of Overall System Pressure Recovery and Total KEP vs. Diffuser Tilt Angle.....	37
Figure 5-7: Inlet Static Pressure Coefficient Distribution for Tilted Diffusers with Flat Wall Collector Box. The Baseline Diffuser-Collector Subsystem is shown for Reference in Orange.	38
Figure 5-8: Contour Plots Showing the Normalized Exit Velocity of the 4 Different Diffuser Tilt Angles within the Flat Wall Collector Box. Exit Flow is Leaving the Page.....	39
Figure 5-9: A Normalized Vector Plot comparison of the 4 Diffuser Tilt Angles Within the Flat Wall Collector Box.....	40
Figure 5-10: Zoomed in Section View of the Baseline Diffuser-Hub Showing the Exit Height of 1.143" known as (h) and the Radius of the Diffuser Shroud (r) for Calculating Radial Hardware Ratios (r/h).	41
Figure 5-11: a) Section View of the r/h=1.0 Radial Diffuser Hardware Components. b) Radial Hubs and Adapter Piece with O-ring shown to Scale by a Quarter.....	42
Figure 5-12: Radial Diffuser Hardware with Pinch Collector Analysis of Overall System Pressure Recovery and Total KEP vs. Diffuser r/h value. The r/h Value of Zero Represents the Baseline Case.	44
Figure 5-13: Inlet Static Pressure Coefficient Distribution for Radial Hardware Designs with Pinch Collector Box. The Baseline Diffuser Collector Subsystem is shown for Reference.	45
Figure 5-14: Contour Plots Showing the Exit Velocity of the 4 Different r/h Radial Diffuser Hardware Designs within the Pinch Collector Box. The Baseline Diffuser Collector Box is also shown for Comparison. Flow Exiting the Collector Box is Out of the Page.....	46
Figure 5-15: Normalized Vector Plot of the Radial Diffusers. Baseline Geometry Included for Reference.....	47
Figure 5-16: a) Surface Oil Flow Visualization of the r/h=1.0 Radial Hub and Back Wall. b) Separation line at the 180 Degree Location of the Hub.	48

Figure 5-17: a) Experimental Setup of the $r/h=1.0$ Radial Diffuser Inside the Flat Wall ECB with the Back Wall and Hub Removed. b) Flow Separation Shown on the $r/h=1.0$ Radial Diffuser Shroud.....	49
Figure 5-18: Surface Oil Flow Visualization of the Flat Wall Collector Using the $r/h=1.0$ Radial Hardware	50
Figure 5-19: a) Cutback Radial Diffuser Design Shown in Solidworks. b) Radial Diffuser Comparison shown within the ECB c) Section View of the $r/h=0.25-1.0$ Cutback Radial Diffuser Inside of the Flat Wall Collector.....	51
Figure 5-20: Circumferential Inlet Static Pressure Coefficient Distribution of $r/h=1.0$ radial diffuser and the Radial Cutback Design. Baseline Configuration is shown for Reference.	52
Figure 5-21: Contour and Vector Plot Comparison of the Baseline, $r/h=1.0$, and Cutback Radial Designs	53
Figure 5-22: Oil Flow on the $r/h=1.0$ Radial Hub Incorporating the Cutback Radial Diffuser	54
Figure 5-23: Oil Flow Visualization of the $r/h=0.25-1.0$ Cutback Radial Diffuser Shroud.....	55
Figure 5-24: Flow in the Bottom Portion of the Flat Wall Collector Using the Radial $r/h=0.25-1.0$ Diffuser.....	55
Figure 5-25: a) CAD Isometric Section View of the Baseline Diffuser Only Test. b) Experimental Setup of the Baseline Diffuser Test with Radial Traverse. c) Experimental Setup of the $r/h=1.0$ Radial Diffuser Hardware with Radial Traverse.	56
Figure 5-26: Plot of the Pressure Recovery versus the Diffuser r/h Value. Baseline Diffuser and Diffuser-Collector Lines added for comparison Purpose.....	57

INDEX OF TABLES:

Table 3-1: Table of Instrumentation Accuracies Provided by the Manufacture	19
Table 3-2: Table of Uncertainties of Performance Variables Using the Jitter and Student t Analysis	19
Table 4-1: Experimental Diffuser Inlet Performance Parameters with Overall Baseline Diffuser-Collector Geometry Performance Values.	23
Table 5-1: Inlet Performance Parameters and Overall Performance Values of the Flat Wall Collector Compared to the Baseline Pinch Collector.....	31
Table 5-2: Tilted Diffuser Performance Table with Flat Wall Collector Showing Experimental Inlet Run Conditions, Pressure Recoveries, and KEP Values.	36
Table 5-3: Radial Diffuser Hardware Design Performance Table with Pinch Collector Showing Experimental Inlet Run Conditions, Pressure Recoveries, and KEP Values.	43

Table 5-4: Performance Table Showing Experimental Inlet Run Conditions, Pressure Recoveries, and KEP Values. Comparing the r/h=1.0 Radial Diffuser with Pinch Collector to the Cutback Radial Diffuser with Flat Wall ECB. The Baseline Configuration is shown for Reference 52

INDEX OF EQUATIONS:

Equation 2-1..... 11
Equation 2-2..... 11
Equation 2-3..... 11
Equation 2-4..... 11
Equation 2-5..... 11
Equation 3-1..... 16
Equation 3-2..... 17
Equation 3-3..... 17
Equation 3-4..... 17
Equation 3-5..... 18
Equation 3-6..... 18
Equation 3-7..... 19
Equation 3-8..... 19
Equation 4-1..... 26

NOMENCLATURE:

Acronyms

CAD	Computer Aided Design
CFD	Computational Fluid Dynamics
CFM	Cubic Feet Per Minute
CMM	Coordinate-Measuring Machine
ECB	Exhaust Collector Box
HPT	High Pressure Turbine
KEP	Kinetic Energy Parameter
LPT	Low Pressure Turbine
MAX	Measurement & Automation Explorer
PIV	Particle Image Velocimetry
PSIA	Pound-Force Per Square Inch Absolute

PSID	Pound-Force Per Square Inch Differential
PSIG	Pound-Force Per Square Inch Gauge
RPM	Revolutions Per Minute
SLA	Stereolithography Rapid Prototyping
SLS	Selective Laser Sintering

Greek

α	Kinetic Energy Flux Velocity Profile Parameter
β	Porosity of a Perforated Plate
δ	Uncertainty
Δ	The Change in Value
γ	Specific Heats Ratio
ρ	Fluid Density

Variables

A	Area
C	Turbulence Intensity Constant
C _p	Pressure Recovery
C _{p_o}	Coefficient of Total Pressure
C _{p_s}	Coefficient of Static Pressure
D	Hole Diameter in a perforated Plate
d _e	Effective Value of Grid Width for a Perforated Plate
Exp	Experimentally Acquired Value
Ma	Mach Number
P _s	Static Pressure
P _t	Total Pressure
P _{var}	Performance Variable
R _d	Reynolds Number Based on Inlet Diameter
S	Distance Between Holes in Perforated Plate
t	Thickness of a Perforated Plate
TU	Turbulence Intensity Value
U	Fluid Velocity
x	Distance Between Perforated Plate and Diffuser Inlet Plane

Subscripts

1	Upstream Location
2	Downstream Location
assumed	Assumed Value
avg _y	Mass Averaged Velocity in the “y” Direction
ext	Measurement Taken at the Exit Plane of the Collector
in	Measurement Taken at the Inlet Plane of the Diffuser
m	Measured Value
offset	Manufacture Provided Accuracy Value
x	Direction Parallel with the Diffuser Centerline
y	Direction Vertically Perpendicular with the Diffuser Centerline
z	Direction Horizontally Perpendicular with the Diffuser Centerline
tot	Magnitude Incorporating All Three (3) Velocity Directions

Accents

—	Time, Mass, and Radial Averaged Data
=	Time, Mass, Radial, and Circumferential Averaged Data

An axial flow gas turbine system is a power generating machine comprised of multiple in-line components each responsible for performing a specific task. In general, a multi-stage compressor is placed at the inlet of the machine to systematically raise the pressure of the incoming ambient air axially throughout each stage. Once the air is pressurized, it is mixed with fuel and ignited in the combustor section which generates an output of hot gases containing high energy levels. Finally, kinetic energy is extracted out of the flow by passing through a series of blades fixed to a shaft within a high pressure turbine (HPT) used to power the compressor. Additional energy in the flow downstream of the HPT is extracted by a low pressure turbine (LPT) which turns a power shaft, thus providing work output. Based upon on the application, the axial flow gas turbine system may have certain space confinements as typically seen in industrial use. Therefore, the exhaust gases leaving the last blade row of the LPT must often be rerouted 90 degrees from the common centerline axis in the upward vertical direction. This crucial turn in flow from the axial to radial direction is made possible by the use of a diffuser-collector subsystem placed downstream of the LPT, as depicted in Figure 1-1.

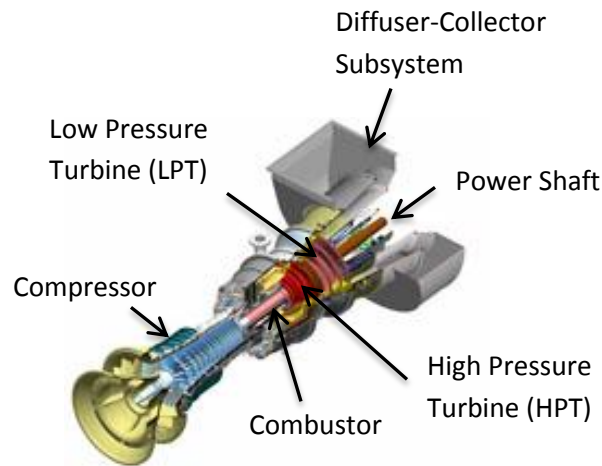


Figure 1-1: Cut-Away View of the Fundamental Components of an Axial Flow Gas Turbine System. Solar Turbines Inc. Used with Written Permission.

1.1: Background of a Gas Turbine Diffuser

A diffuser is commonly placed downstream of the last turbine blade row to capture the remaining high velocity, high temperature exhaust gases before being released into the atmosphere. Geometrically, a diffuser is a simple fluid-mechanical device that has an increasing area ratio from inlet to exit that extends a certain axial length. Its primary purpose is used for slowing down fluid flow while simultaneously increasing static pressure, thus exchanging kinetic energy for a pressure rise. In an ideal case, the turbine outlet total pressure would be equal to the diffuser's exit static pressure, signifying that the exhaust flow has fully expanded and come

to rest. This would result in a full pressure recovery. In reality, the diffuser inlet total pressure will be higher than the diffuser exit static pressure due to the diffuser geometry as well as the inflow conditions [(Vassiliev, Rothbrust, & Irmisch, 2008)]. The difference in pressure between the diffuser outlet (ambient) and the gas turbine exhaust is referred to as exhaust loss. The trade-off from dynamic to static pressure is the primary objective of the diffuser which results in a reduction of back pressure on the turbine allowing for an increased expansion ratio, thereby increasing its power output [(Sovran & Klomp, 1967)].

1.1.1: Previous Diffuser Research

Sovran & Klomp (1967) published a definitive work on diffuser performance in 1967 by studying the performance characteristics of three common types of straight-walled diffusers; 2-D rectangular, conical, and annular. Uniform inlet flow conditions with small area blockage, and no swirl distribution were used in the analysis. Multiple performance charts were created to show diffuser pressure recovery as a function of non-dimensional diffuser length or area ratio. Sovran and Klomp's research remains a valuable reference as it helps to determine the most efficient diffuser based on an optimum geometry.

Hoffmann (1981) studied the effects of free-stream turbulence on a subsonic two-dimensional diffuser by using a variation of equally spaced rod sets to generate different inlet turbulence parameters. The inlet Reynolds number was held constant at 7.83×10^4 for all experimental tests. This study found that free-stream turbulence greatly affects the turbulence intensities within the boundary layer without significantly altering the boundary layer velocity profile at the diffuser inlet. With the rods perpendicular to the flow and parallel to the diffuser's diverging walls, the diffuser's static pressure recovery coefficient was increased. It's believed that the specified orientation of the eddies transmits the free-stream energy to the diffuser's walls more effectively, thus delays the separation within the diffuser and increases performance.

Vassiliev, Rothbrust, & Irmisch (2008) aerodynamically optimized an industrial gas turbine diffuser to compensate for an increased mass flow. Radial traverse measurements at the diffuser inlet of a test engine were taken using two 5-hole probes located at two different circumferential positions. Numerical analysis was performed to identify improvement measures of the original diffuser and to validate performance parameters of new diffuser design. It was determined that the flow straightening plates used to minimize residual swirl at the diffuser outlet be removed due to flow separation along the plates causing a reduction in pressure recovery. The support struts were also redesigned to align with the inlet swirl angle, minimizing local separation and reducing exhaust loss. A scaled model of the optimized diffuser was tested in a test rig designed to match the inlet swirl angle of the real engine. The results showed a 30% reduction in exhaust loss signifying a successfully optimized diffuser design.

1.2: Background of a Diffuser-Collector Exhaust Box

The collector box is the furthest downstream component in an axial industrial gas turbine system. It can vary in many different shapes, sizes, and internal features depending on the specific application. A typical collector box is designed with a single inflow to accept expanding turbine exhaust gases from the diffuser exit and a single outflow exhausting to atmosphere. When coupling an efficient diffuser to a collector box, the diffuser performance deteriorates due to early flow separation from its inner walls. Furthermore, the back wall of the collector box effectively reduces the out-flow area creating a back pressuring effect on the LPT and the formation of detrimental secondary flows within the collector box. A portion of this study verifies previous research that two strong counter-rotating vortices exist inside the exit section of the exhaust collector box, ultimately increases the total pressure loss and decreases turbine performance.

1.2.1: Previous Diffuser-Collector Research

(Samal, 2011): A quarter-scale diffuser-collector subsystem was built and tested by Techsburg, Inc located in Christiansburg, VA. The full-scale production geometry was provided by Solar Turbines in San Diego, CA. This research was successful in evaluating the Solar Turbines diffuser-collector design through the use of pressure measurements, traverse measurements, and stereo PIV. It was found that flow within both the collector and the diffuser, were strongly dependent on the exhaust collector box geometry. Two large counter rotating vortices were verified through the use of stereo PIV and were presumed to cause a drop in overall pressure recovery. Further testing and experimentation was recommended in order to properly evaluate the effect of the exhaust collector box geometry upon the pressure recovery and flow development.

Bernier, Kapat, & Ricklick (2011) investigated the effects of an industrial gas turbine exhaust collector box geometry on static pressure recovery and total pressure loss. The exhaust diffuser and uniform inlet velocity profile were held constant for each collector box geometry. Experimental results show that by increasing the distance between the exit of the diffuser and the collector back wall, the two strong counter rotating helical vortices were weakened and the total pressure loss was decreased by 19% for this particular investigation. Furthermore, the exhaust collector box proved to cause early separation within the diffuser due to the recirculation off the back wall of the collector, thus decreasing the diffuser pressure recovery.

(Zhu, Wang, & Du, 2010): The aerodynamic performance of a low pressure turbine exhaust hood was optimized by utilizing the Matlab platform and the commercial CFD simulator CFX. Four modules were introduced into the system; the geometry parameterization, the commercial mesh generator Icem-CFD, the commercial CFD aerodynamic simulator CFX, and the Kriging surrogate adaptive optimizer. The Kriging surrogate model was used to establish a

global mapping between design variables and the overall objective function. The optimization objective function was defined as the mass averaged pressure recovery coefficient. The results show that the optimization of a low pressure turbine exhaust hood could be validated by using the Kriging surrogate model. Furthermore, contour maps showing the turbulence kinetic energy, the total pressure loss coefficient, and the static pressure coefficient were generated, illustrating the validation of the improved performance compared to the original design.

1.2.2: Diffuser-Collector Subsystem Patents

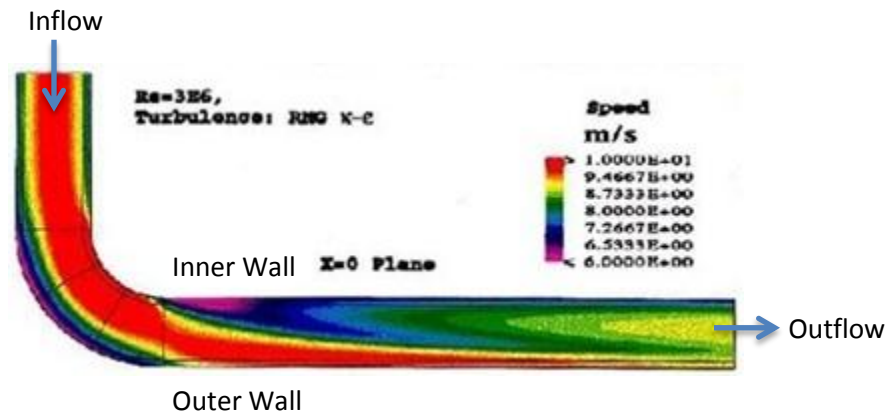
Hardin (2010) obtained patent (US7731475) for the invention to tilt the exhaust annular diffuser towards the exit section of the exhaust collector box which turned exhaust gases 90 degrees from the longitudinal axis of the turbine shaft. The diffuser tilt claimed to create a more uniform circumferential pressure recovery compared to a conventional non-tilt exhaust system. A range of 3 to 7 degrees was specified for the diffuser tilt angle with 5 degrees considered as the optimum.

Nanda, Pruthi, & Ansari (2012) obtained a patent (US20120034064) for a gas turbine diffuser that incorporates an axial diffuser section, an axial-radial diffuser section, and a radial diffuser section, thus eliminating the need for any internal turning vane. It's claimed that by coupling these multiple diffuser sections, a smooth flow path to transition the flow from the axial to radial direction is achieved while maximizing the pressure recovery in the diffuser. Furthermore, the entire exhaust diffuser cross-sectional area expands downstream from inlet to outlet, resulting in continuous diffusion and reduced pressure loss.

(Takamura, 1983): A patent (US4391566) was allowed based on a diffuser-collector gas turbine arrangement to suppress formation of vortex flows inside the gas collector chamber based on two designs. The first design used a pair of ribs attached to the outer wall member of the diffuser which protruded towards the exit of the collector box. Experiments were shown that for optimal performance the ribs be inclined at an angle between 90 to 55 degrees. The exhaust gases are guided along the ribs toward the exit section of the collector preventing the formation of detrimental vortices inside the collector. The second design incorporated an annual flange at the exit of the diffuser which projects radially outward a known distance. The primary purpose is to serve as a flow stabilizer while also keeping the production cost of the gas turbine low due to its simple diffuser wall member modification. It's claimed that these simple modifications will minimize vortex formations, reducing the back pressure in the power section of the engine, thus increasing the pressure recovery of the system and generating more power.

1.3: Fundamental Fluid Flow in 90 Degree Bends and of Impinging Jets

Some of the basic flow structures and patterns exhibited within the complex experimental diffuser collector subsystem relate back to the fundamental fluid flow within common geometries.



<http://www.f1technical.net/forum/viewtopic.php?f=6&t=9813&start=60>

Figure 1-2: Fundamental CFD Model of Fluid Flow Velocity within a 90 Degree Elbow

Sudo, Sumida, & Hibara (1998) experimentally analyzed the turbulent flow structure within a circular sectioned 90-degree bend. The static pressure was measured on the pipe wall upstream, downstream and within the 90 degree bend while velocity measurements were made by rotating a single inclined hot wire. Results show that the flow upstream of the bend is not yet influenced thus providing concentric circle contours. Once the flow enters the inlet plane of the bend, the fluid is slightly accelerated near the inner wall and decelerated near the outer wall due to the respective favorable and unfavorable longitudinal pressure gradients. At approximately 30 degrees in the bend, the well-known counter-rotating vortices form over the entire cross section due to the centrifugal force causing fluid to circulate outwards in the middle part of the pipe and inwards near the upper and lower walls. At around 60 degrees in the bend, the secondary flow moves the faster moving fluid near the inner wall towards the outer wall utilizing the central portion of the pipe. In effect, the slower moving fluid at the pipe's upper and lower walls is brought towards the inner wall due to the secondary flow. This causes the pressure to rise in the longitudinal direction, decelerating the flow near the inner wall. The fast, primary fluid moves towards the outer wall and the secondary flow grows rapidly. Between 75 to 90 degrees in the bend, the primary velocity contours are distorted and a depression is formed between the inner wall and the center region of the bend due to the outward secondary flow. At the exit of the 90 degree bend, the fluid velocity is fastest at the outer wall and the secondary flow becomes its strongest. As the flow continues further

downstream of the exit plane of the bend, the primary velocity distribution gradually becomes smooth, the secondary flow weakens, and the vortices breakdown to near straight pipe flow conditions. Similar fluid flow phenomena can be seen in 90 degree square cross section bends as well [(Sudo, Sumida, & Hibara, 2001)]. A cross-section view of this flow structure within a 90 degree elbow is shown in Figure 1-2 above.

Camci & Rizzo, (2001) studied the effects of secondary flow and heat transfer in a 90 degree turned square duct using 6 different endwall boundary layer fence configurations including a baseline non-fence case. The fences were placed on the heated endwall midway between the pressure and suction surfaces in an attempt to reduce the secondary kinetic energy of the passage vortex flow near the endwall. The inlet boundary layer was set fully turbulent with the Reynolds number equal to 3.6×10^5 . It was shown through use of various contour plots that the viscous losses in the duct were associated with total pressure losses concentrated in the passage vortex region. A high loss core was generated on the suction side at the exit of the 90 degree turning duct with a counter rotating passage vortex on either side. All fence designs were shown to weaken the secondary flow within the square duct compared to the non-fence case. The fence dimensions could be optimized based on a trade-off between the addition of viscous and mixing losses due to the fence and the beneficial reduction in losses due to weakening the passage vortex.

Moller (1966) investigated geometry and flow parameters important in the design of an efficient, incompressible-flow, radial diffuser impinging on a flat plate. It was found that the pressure recovery became nearly independent of Reynolds number for $R_d > 2 \times 10^5$. For Reynolds numbers less than that value, the pressure recovery rapidly decreased and fell below the theoretical prediction. This prediction assumed having thin boundary layers at the inlet of the diffuser and no flow separation from the walls. Further experimental results showed a similarity of pressure recovery between the radial diffuser and a 7-degree conical diffuser at high Reynolds numbers. Multiple optimum performance charts were created from experimental data as a function of Reynolds number, area ratio, and radial diffuser channel width. All of the experimental results were based on swirl-free flow.

The previous research and patents mentioned above helped to provide a general understanding of the complex secondary flow structures present inside the diffuser-collector subsystem. These structures include the counter rotating vortices at the exit section of the collector as well as the back pressuring effects seen at the exhaust of the low pressure turbine. Unfortunately, there is a limited amount of research performed on the crucial diffuser-collector subsystem as to why these detrimental flow structures exist and how the specific geometry causes such issues. This paper was created to demonstrate the relationship between specific diffuser-collector geometries and the overall gas turbine performance.

The research performed in this study took place at Techsburg Inc., located in Christiansburg, VA. This research concentrates on the design and the effects of coupling both a diffuser and an exhaust collector box into a complete subsystem, turning the fluid 90 degrees from the common centerline axis while providing an optimum overall pressure recovery. The basis for minimizing secondary flow within the collector box was studied using interchangeable geometries and discovered trends.

Chapter 2 - Small Scale Diffuser-Collector Research Facility Purpose and Design

A small scale wind tunnel facility was constructed to support the testing of various diffuser-collector geometries at the one-twelfth scale. This small scale design played an important role in the optimization of performance parameters from multiple diffuser-collector subsystem geometries in a time-efficient and cost effective manner. This research facility allowed for easy to handle components, quick experimental testing, and time-efficient accurate results. Utilizing these benefits, a better understanding of the complex 3-D fluid structure within each diffuser-collector subsystem geometry was obtained; Providing valuable results towards the next best optimum geometry design.

All experimental testing was performed using a blower to supply continuous air into the diffuser-collector subsystem, at a near constant mass-flow rate. PVC schedule 80 piping was used to channel the air either towards the test article or through a ball valve used to regulate any necessary facility bleed. A pipe flow conditioner was placed upstream of the contraction flange to set the appropriate inlet flow characteristics. The air from the exit section of the collector box was positioned to exhaust in the upward vertical direction to atmosphere.

2.1: Busch Panther Continuous Blower

A Busch Panther blower WA3125DP was selected as the source for continuous air displacement through the diffuser-collector test article. The electric blower is a rotary lobe, positive displacement blower capable of discharging 1571 Cubic Feet per Minute (CFM) at 2850 Revolutions per Minute (RPM) based on ambient conditions of 14.7 psig and 70°F [(Busch Inc.)]. For this research, the blower was designed to produce an inlet Mach number of 0.42 matching the full scale diffuser collector production model. The continuous operation blower can see below in Figure 2-1.



Figure 2-1: Busch Panther WA3125DP Continuous Blower with the Inlet and Outlet Locations Labeled

2.2: Wind Tunnel Ductwork

The duct-work downstream of the blower outlet consisted of several 6 and 8 inch PVC schedule 80 components. These components were responsible for both translating the flow from the height of the blower outlet to the height of the diffuser-collector test section and to direct flow through a single 6 inch PVC ball valve used for regulating the mass flow rate of the facility. For all experimental runs, the ball valve was placed in the fully closed position, eliminating facility bleed. A pipe flow conditioner was placed between the straight section of the blower (supplying turbulent exhaust air) and the inlet of the contraction flange to provide the necessary uniform flow conditions for experimental testing.

2.2.1: Pipe Flow Path and Material

An eight-hole pattern 6 inch flange was used to connect the blower exhaust flow to a short 16 inch straight pipe section. This section extended axially along the common centerline of the blower outflow to a 6 inch 90 degree elbow. The elbow was used to translate the flow from the axial to radial direction, thus increasing the height from the blower outflow to the center of the test article approximately 38 inches from ground level. The radial outflow from the elbow entered into a 6 inch "T" section which continued the radial flow through a 6 inch ball valve or if the valve was shut, turned all of the flow in the axial direction towards the diffuser collector box. A 6 to 8 inch pipe expander was used to connect the axial flow from the "T" section to an 8 inch 5 foot long pipe that bolted to an existing 8 inch 2 foot long metal pipe flow conditioner section. The exhaust flow from the pipe flow conditioner was bolted to an 8 inch contraction flange which served as the most upstream flow conditioning component for the diffuser-collector assembly.



a



b

Figure 2-2: a) Individual PVC Schedule 80 Piping Components. b) Flow Path of the Assembled PVC Components Attached to the Blower Exhaust.

2.2.2: Pipe Flow Conditioner

To provide a uniform velocity profile at the inlet of the contraction flange, a two foot long straight metal pipe consisting of honeycomb and four half inch thick metal discs containing mesh screens in the inner diameter were used in the design. The honeycomb and mesh screens were placed upstream of the pipe section to evenly distribute and straighten the flow before traveling down to the contraction flange. The experimental pipe flow conditioner is shown in Figure 2-3 below.

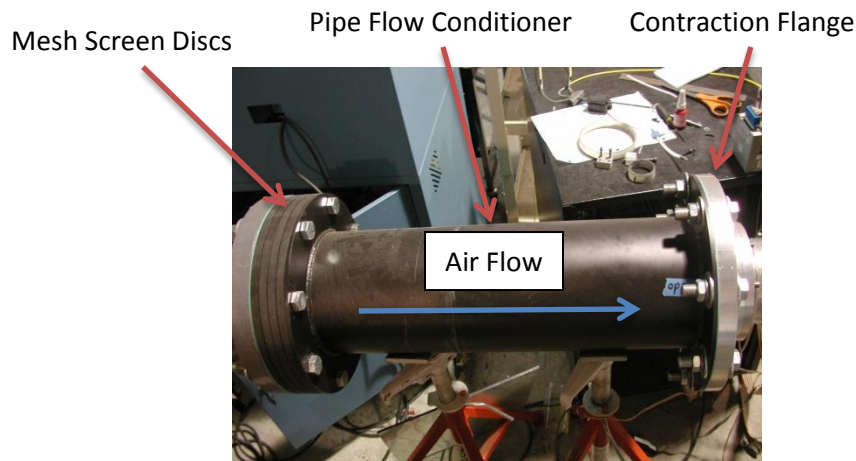


Figure 2-3: Pipe Flow Conditioner Placed Upstream of the Contraction Flange. The Four (4) Metal Discs Containing Mesh Screens are labeled.

2.3: Design and Configuration of the Inlet Flow Conditioning Components

In the full-scale production model, the diffuser-collector subsystem is designed to accept combustion products from the exhaust of the gas turbine engine. Therefore, in order to create similarity between the full scale operation and the twelfth scale continuous blower research, several components had to be inserted upstream of the diffuser-collector test article. By adding a turbulence grid, swirl vanes, and a boundary layer contraction section, the inlet flow was then properly conditioned to mimic the flow leaving the last blade row of the low pressure turbine (LPT).

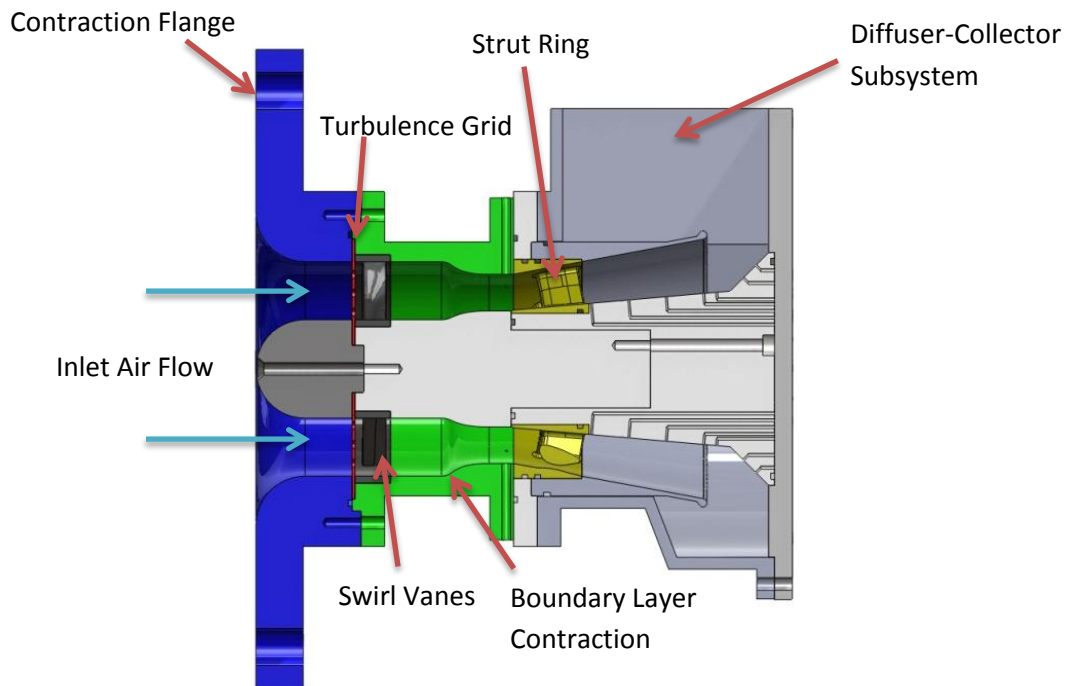


Figure 2-4: Section View of the Flow Conditioning Components Upstream of the Diffuser-Collector.

2.3.1: Large Contraction Flange

A customized contraction flange shown in blue in Figure 2-4 above was built out of aluminum 6061 to serve multiple purposes in the small scale research facility. The primary purpose of the contraction flange was to take the uniformly distributed air from the large exit area of the pipe flow conditioner and smoothly accelerate it down into the annulus of the diffuser-collector flow conditioning section. The approximate contraction ratio of the pipe flow conditioner to the test section annulus is 1.76. The contraction flange was also designed to securely hold the turbulence grid located directly downstream of the flange. Finally, 8 $\frac{1}{4}$ -20 tapped holes were spaced even around the circumference of the extruded contraction along with a special mating groove used to align the boundary layer contraction section shown in green. An O-ring was

placed between the contraction flange and the boundary layer contraction section to ensure a tight fit.

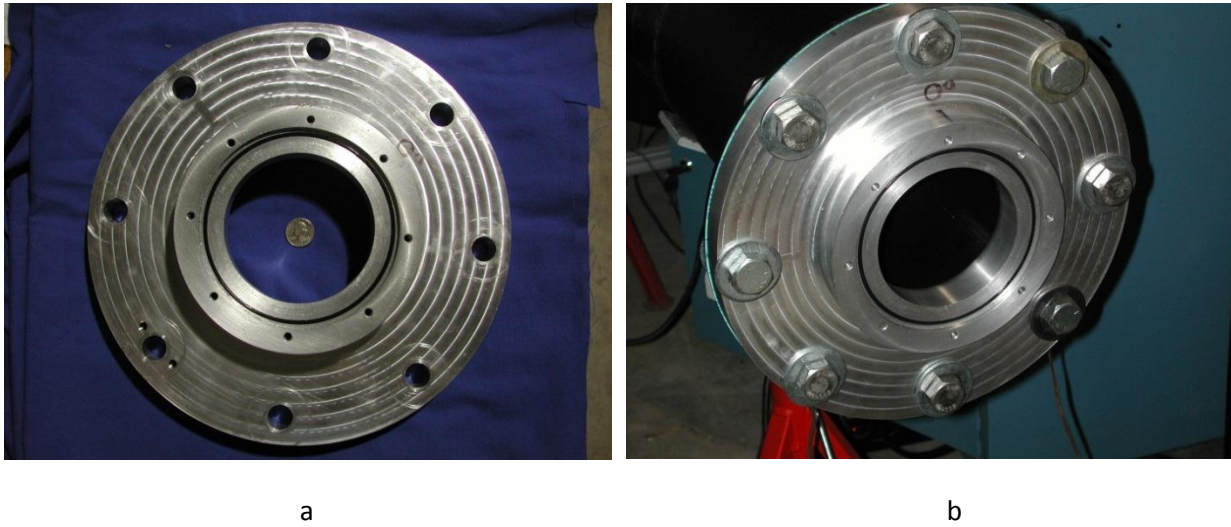


Figure 2-5: a) Contraction Flange Shown to Scale by a Quarter b) Contraction Flange Bolted to Upstream Pipe Flow Conditioner. The O-ring is Shown Installed in Both Pictures.

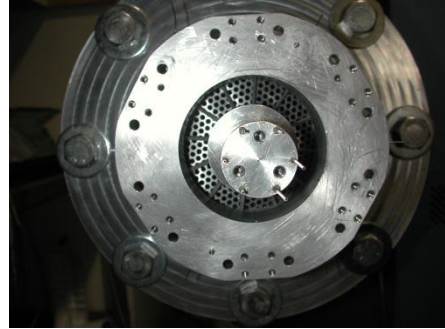
2.3.2: Turbulence Grid

In order to obtain the desired turbulence level at the inlet of the diffuser a 1/16 inch thick porous metal disc was placed upstream of the swirl vanes at the exit of the contraction flange. The porosity of the disc based on the diameter of the holes and their spacing can be found by using Equation 2-1. The turbulence intensity was calculated using Roach’s 1987 paper which relates the downstream turbulence properties of grids to that of using perforated plates. Equation 2-2 is used as a constant relating the perforated plate thickness to the hole diameter ratio. When considering the downstream turbulence properties, the bar width used in the formation of a grid is commonly used, therefore Equation 2-3 provides an effective diameter when using a perforated plate. Equation 2-4 calculates the turbulence intensity by using variables relating to a perforated plate rather than the common grid geometry.

Equation 2-1	$\beta = \frac{\frac{\pi D^2}{4}}{S^2 \cos 30 * 2 \sin 30}$
Equation 2-2	$C = 0.77 \left(\frac{t}{D}\right)^{-0.14}$
Equation 2-3	$de = D \left(\frac{1}{\sqrt{\beta}} - 1\right)$
Equation 2-4	$TU_1 = C \left(\frac{x}{de}\right)^{-5}$
Equation 2-5	$TU_2 = \frac{TU_1}{A_1/A_2}$



a



b

Figure 2-6: a) Turbulence Grid Bolted between the Nose Cone and Hub components. Shown to Scale by a Quarter. b) Upstream View through the Boundary Layer Contraction Section of the Perforated Turbulence Grid.

As the distance between the turbulence grid and the inlet of the diffuser increases, the turbulence intensity decreases in a proportional manner. A 6% turbulence intensity was generated at the inlet of the diffuser by using 0.168 inch diameter holes spaced 0.231 inches apart from one another. The turbulence intensity value was then modified using Equation 2-5 due to the area reduction from the boundary layer contraction section reducing the intensity to around 5.6%.

2.3.3: Swirl Vanes

To properly mimic the flow leaving the last blade row of the LPT, swirl vanes were placed directly downstream of the turbulence grid to set the desired swirl distribution at the inlet of the diffuser. The swirl vane ring was constructed from Selective Laser Sintering (SLS) glass filled nylon 12 material having high strength and temperature deflection properties. The swirl distribution will change based on the turbine operating point. For this small scale research, the operating point was set at 100% speed creating a counterclockwise swirl rotation of between 6 to 7 degrees at the inlet of the diffuser when looking upstream into the flow. A picture of the swirl vane ring can be seen in Figure 2-7 below.



Figure 2-7: Swirl Vane Ring Made From SLS Rapid Prototyping Shown to Scale by a Quarter.

2.3.4: Boundary Layer Contraction

A boundary layer contraction section (green) was placed between the exit of the contraction flange (blue) and the inlet to the diffuser (yellow) as shown in Figure 2-8 below.

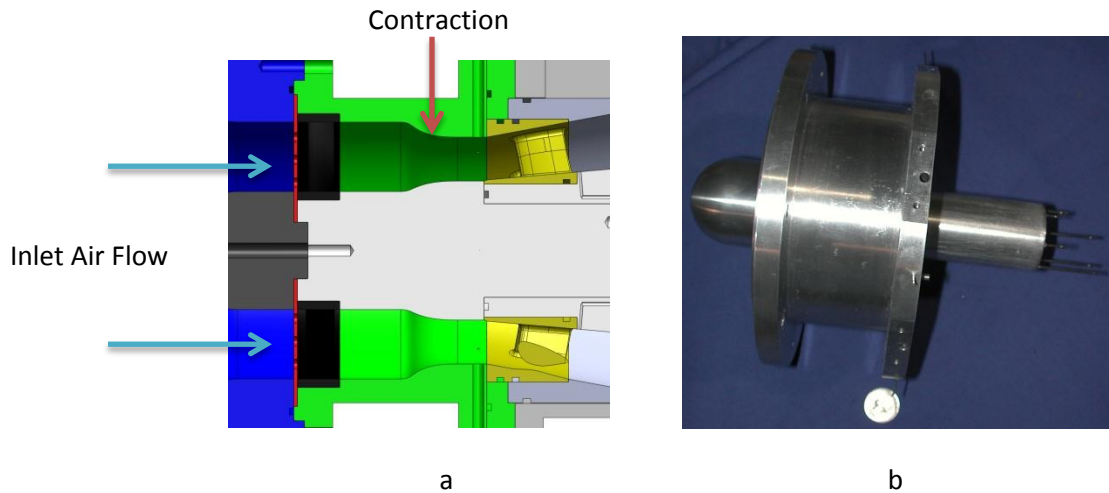


Figure 2-8: a) Zoomed in View Showing the Boundary Layer Contraction Colored in Green. b) Sub Assembly of the Boundary Layer Contraction Section Scaled by a Quarter.

This contraction was used to achieve the desired boundary layer profile, thus providing the necessary pressure and velocity distributions at the inlet of the diffuser. The contraction provided a flow area ratio of 1.617.

2.3.5: Struts

A strut ring was fabricated out of the same SLS rapid prototyping material as the swirl vanes and was placed within the allocated slot at the inlet of the diffuser. The strut ring was designed to have the same expansion ratio as the diffuser, thus providing a smooth constant flow expansion through both components. Every diffuser design incorporated the same size strut ring slot providing easy diffuser interchangeability and reuse of the strut ring. The outside of the ring was designed with two circumferential grooves for O-ring placement, one between the case and the other between the diffuser. The struts provided support of the center body while also acting as a de-swirler at the inlet of the diffuser by utilizing its eleven evenly spaced NACA airfoils.

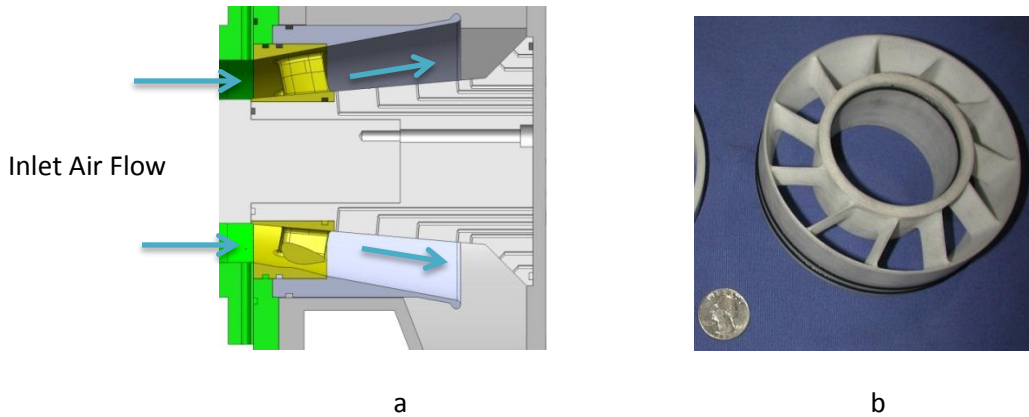


Figure 2-9: a) Section View of the Strut Ring (yellow) Assembled Having Equivalent Expansion Ratio as the Diffuser. b) Nylon SLS Strut Ring Scaled by a Quarter with O-rings Installed.

Chapter 3 - Instrumentation, Data Acquisition, and Processing

3.1: Data Acquisition Software & Temperature/Pressure Hardware

The small scale diffuser-collector research facility used an existing Techsburg Labview program to precisely acquire, calculate, and record time averaged temperature and pressure values at a user defined rate and length of time. The program was set to record a total of 3,200 samples taken within a 4 second time span. Furthermore, this program provided the capability to control a stepper motor used to traverse a pressure probe to various radial heights within the test article. The probe was traversed to an accuracy of within one one-thousandth of an inch. A screen shot of the program can be seen in Figure 3-1(a) below:

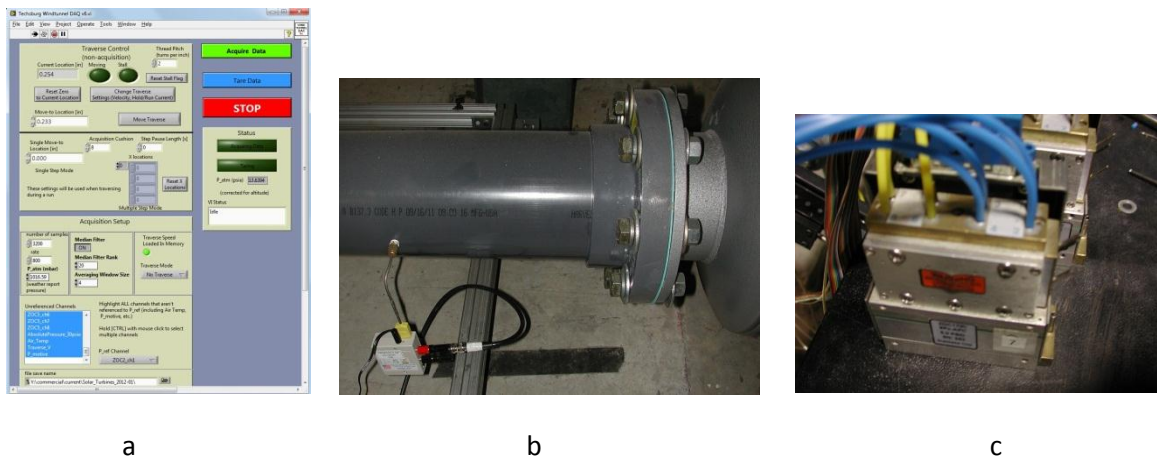


Figure 3-1: a) Labview Program used for Acquiring Time Averaged Data and Stepper Motor Traverse Control. b) Thermocouple Placed at the Exhaust of the Blower. c) Scanivalve Corp ZOC17 8-Channel Pressure Transducer.

The total temperature was measured within $\pm 7.2^\circ$ F by using an Omega TAC80B-K thermocouple located at the exhaust of the blower as seen in Figure 3-1(b). The temperature was tracked live through the use of National Instruments Measurement & Automation Explorer (MAX) program. As the blower ran, the temperature increased as a function of time. Data was not acquired until the temperature reached a steady state value of approximately 130 degrees Fahrenheit.

Both total and static pressure were measured within ± 0.000325 psid by using Scanivalve Corp ZOC17 5.0 psid pressure transducers. The pressures were recorded from static pressure taps located on both the case and hub and/or pressure probes that were traversed in the flow. Each active pressure transducer channel was connected to a pressure port using .125 x 0.062 inch polyethylene tubing as shown in Figure 3-1(c) above.

3.2: Diffuser Inlet Measurements

The flow characteristics at the diffuser inlet were measured by using a combination of static pressure taps in conjunction with a three-hole wedge probe for radial traversing. Six static pressure taps located directly upstream of the strut ring (inlet to the diffuser) were placed through both the case and hub to provide an inlet circumferential static pressure distribution profile. Radial traverse holes were drilled through the boundary layer contraction flange to provide access for the United Sensor 3/16" WAC-187 three-hole probe. This wedge shaped 2D directional probe provided inlet swirl angle, total pressure, and static pressure by using its three triangular spaced pressure ports insensitive to pitch angles up to 30° [(United Sensor Corp., 2011)]. The probe access holes were placed in the boundary layer contraction flange every 60 degrees referenced to the 12 o'clock location as shown below in Figure 3-2. Special plates and pins were used to block any air flow through the traverse access holes when the probe was not present. Each plate was equipped with a small O-ring and two #6-32 screws to provide a tight seal between the bottom portion of the plate and the flat surface of the boundary layer contraction flange.

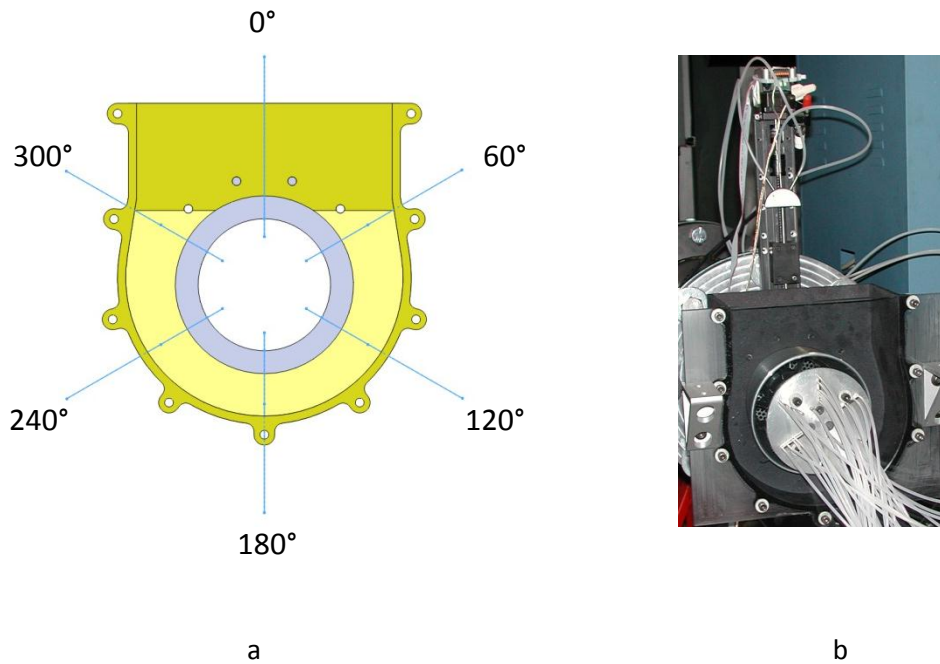


Figure 3-2: a) An Upstream View of the Circumferential Radial Traverse Locations in Reference to the Pinch Collector Box. b) Experimental Setup of a Radial Traverse Using the 3-hole Wedge Probe at the 0° Location.

At each circumferential location, the probe was traversed at 5 different radial heights inside the annulus ranging from 30 to 70 percent of the entire case to hub radial distance. Each radial measurement was taken in 10 percent increments within the given traverse range. Once all of the pressures were acquired at each circumferential location, the data was then combined and linearly interpolated to form a diffuser inlet flow profile. By using each radial traverse position, a mass average value was determined at every pointwise location. These mass averaged values were used to calculate different inlet flow parameters such as Mach number, total pressure, static pressure, and swirl angle.

A single Mach number at the inlet of the diffuser was calculated by using the mass average static and total pressure values. These pressure values incorporate all 5 of the radial traverse measurements at each of the 6 circumferential locations.

Equation 3-1	$Ma_{in} = \sqrt{\frac{2}{\gamma-1} \left[\left(\frac{\overline{P}_{t_{in}}}{\overline{P}_{s_{in}}} \right)^{\frac{\gamma-1}{\gamma}} - 1 \right]}$
--------------	---

The pressure recovery of the overall diffuser-collector subsystem was calculated based on the same mass average total and static pressures. The definition of pressure recovery relates the actual static pressure rise to the maximum theoretical (ideal) pressure rise, thus equating to a number less than 1. This value was used to quantify the overall efficiency of the diffuser-collector subsystem.

Equation 3-2	$Cp = \frac{(\overline{P}_{S_{ext}} - \overline{P}_{S_{in}})}{\overline{P}_{t_{in}} - \overline{P}_{S_{in}}}$
--------------	---

The total and static pressure coefficients for each circumferential location were calculated by radially averaging the mass average pressure values. The measured pressure value was then normalized by the inlet dynamic pressure calculated from the mass average total and static pressure.

Equation 3-3	$Cp_o = \frac{\overline{P}_{t_{in}} - \overline{P}_{t_{in}}}{\overline{P}_{t_{in}} - \overline{P}_{S_{in}}}$
--------------	--

Equation 3-4	$Cp_s = \frac{\overline{P}_{S_{in}} - \overline{P}_{S_{in}}}{\overline{P}_{t_{in}} - \overline{P}_{S_{in}}}$
--------------	--

3.3: Collector Exit Section Measurements

Just as the inlet of the diffuser was surveyed to create an inlet diffuser profile, a plane located in the exit section of the collector box was also pressure measured to create an exit collector profile. The exit plane located inside of the collector box is shown in green in Figure 3-3 below.



Figure 3-3: a) Isometric View of the Exit Traverse Plane Shown in Green with the Back Wall and Hub Removed. b) Experimental Setup of the Exit Traverse Utilizing Two Stepper Motors and the 5-hole Probe.

Two traverse systems were designed to work in unison to traverse a 5-hole probe in a grid across the exit section of the exhaust collector box. This traverse pattern was automated by modifying the existing Labview program to work with two stepper motors in a nested for-loop. The probe acquired pressure data at a total of 800 points within the collector box by stopping to acquire time averaged data for 4 seconds before moving onto the next point. This exit traverse utilized an Aeroprobe 3D directional 5-hole probe with an angular limitation between 55 to 60 degrees [(Aeroprobe Corp., 2006)]. The 5 raw pressure values along with the total temperature value for each point were properly formatted and imported into Aeroprobe’s Multiprobe software. The software provided an export file of all three velocity directions (u, v, and w) along with additional flow parameters such as Mach number, Reynolds number and density for each of the 800 traversed locations. In order to evaluate uniform flow within the traversed exit area of the collector box, Kinetic Energy Parameter (KEP) values were calculated.

Equation 3-5	$\alpha_y = \frac{1}{A} \int^A \left(\frac{U_y}{U_{avg,y}} \right)^3 dA$
--------------	---

Equation 3-6	$\alpha_{tot} = \frac{1}{A} \int^A \left(\frac{(U_x^2 + U_y^2 + U_z^2) U_y}{U_{avg,y}^3} \right) dA$
--------------	---

The kinetic energy flux velocity profile parameter equations above compare via ratio the actual kinetic energy flux at the collector box cross section exit area to the minimum (uniform) kinetic energy flux which could exist at the particular flow rate [(Sovran & Klomp, 1967)]. Equation 3-5 calculates the KEP value by only looking at the radial velocity leaving the collector box (Uy) while Equation 3-6 incorporates all three velocity directions (Ux, Uy, Uz). The more non-uniform the velocity is across the cross section area, the greater α will be from one.

In addition to the KEP values, a mass averaged velocity for each direction (Ux, Uy, Uz), static and total pressures, and Mach number were calculated at the exit traverse plane. A variety of contour and vector plots were also generated using Fieldview software as a post-processing graphical analysis tool.

3.4: Uncertainty Analysis

In order gain confidence of the experimental results obtained from the 1/12 scale facility, two different types of uncertainty analysis were performed using the baseline geometry configuration. One method involved pure numeric computation, while the other incorporated experimental validation. A jitter analysis was implemented on the experimentally measured values based on the manufacture instrumentation accuracy. The amount each measured value

was independently offset is provided below in Table 3-1. Equation 3-7 was used to calculate the ratio of the difference between the measured performance variable and the assumed performance variable (due to the manufacture offset) over the change between the measured experimental value and assumed experimental value. Equation 3-8 used the ratio found from the previous equation and multiplied it by the manufacture offset or accuracy. All the individual uncertainties were summed generating the instrumentation uncertainty of a single performance variable found in Table 3-2.

Table 3-1: Table of Instrumentation Accuracies Provided by the Manufacture

Instrumentation Device	Accuracy (\pm)
Scanivalve Pressure Transducer	0.00325 PSID
Omega Thermocouple	7.2° F

Equation 3-7	$\frac{\Delta_{P_{var}}}{\Delta_{Exp}} = \frac{P_{var_m} - P_{var_{assumed}}}{Exp_m - Exp_{assumed}}$
--------------	---

Equation 3-8	$\delta_{P_{var}} = \sqrt{\sum \left[\frac{\Delta_{P_{var}}}{\Delta_{Exp}} \delta_{offset} \right]^2}$
--------------	---

The second type of uncertainty analysis was performed experimentally. The baseline diffuser-collector geometry was experimentally tested a total of 3 different times. The geometry had been fully disassembled and reassembled to account for any fluctuations in data due to the assembly process. Although the sample size is considered small, a t-distribution was used to compute a 95% confidence interval for various performance variables assuming a normal population distribution. The results of both the instrumentation and experimental (overall) uncertainties are provided below in Table 3-2. The uncertainty is to be calculated based on the raw measured value.

Table 3-2: Table of Uncertainties of Performance Variables Using the Jitter and Student t Analysis

Performance Variable	Overall Uncertainty (\pm)	Instrumentation Uncertainty (\pm)
Inlet Mach Number	1.74%	0.02%
Inlet Corrected Flow, ωc	1.79%	0.02%
Inlet Reynolds Number, Re_{DH}	4.33%	2.96%
Pressure Recovery, C_p	0.12%	0.04%

The original full scale diffuser-collector geometry shown in Figure 4-1(a) was provided by Solar Turbines in San Diego, CA. For experimental purpose, Techsburg incorporated only the necessary flow features in the scaled model by using various simplifications/modifications from the full scale design. Such simplifications included changing the mounting points on the case and hub and ignoring heat expansion joints found in the full scale production model (Samal, 2011). Additional design features were taken from previous Techsburg research of a quarter-scale diffuser-collector subsystem which provided the foundation for this research.

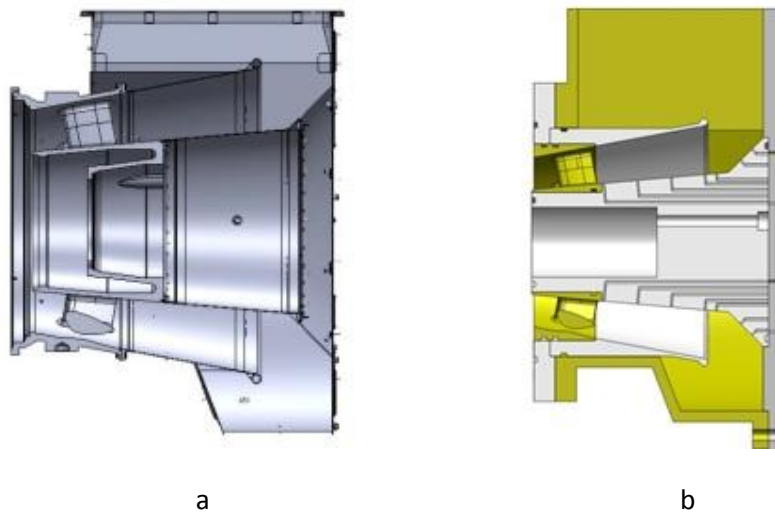


Figure 4-1: a) Section View of the Solar Turbines Full Scale Production Model Geometry. b) Section View of Simplified Experimental One-Twelfth Scale Geometry.

4.1: Experimental Baseline Diffuser-Collector Box Design and Components

The basis of this research began from a diffuser-collector geometry provided by Solar Turbines which consisted of a pinch collector and an annular diffuser, known as the baseline model. In this design, the flow ran in the axial direction expanding through the diffuser and spilling into the open area of the collector. The Exhaust Collector Box (ECB) was designed with an approximate angle of 111.2 degrees between the horizontal and the front wall (known as a pinch) which is illustrated in Figure 4-2(a) below:

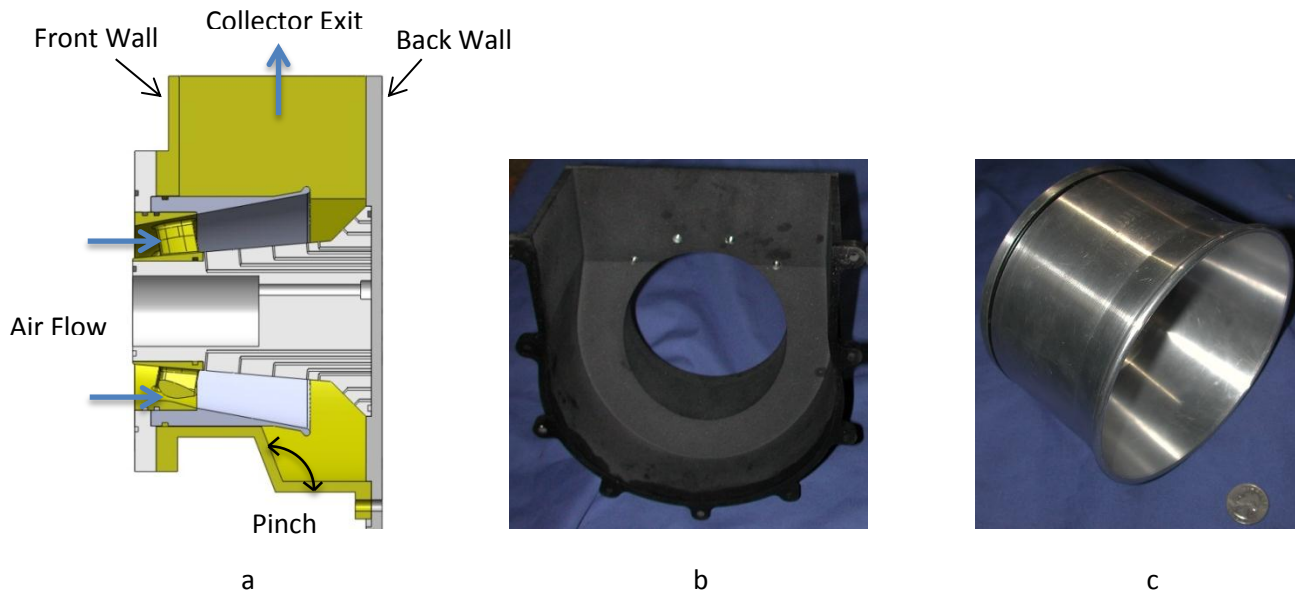


Figure 4-2: a) Section View of the One-Twelfth Scale Baseline Diffuser-Collector Subsystem. b) Experimental SLS Baseline Pinch Collector Box. c) Baseline Aluminum Diffuser Scaled by a Quarter.

The front wall was angled in the pinched collector such that the cross-sectional area inside the collector box decreased moving from the exit plane inwards. This specific geometry design was assumed to help push air up and out from the bottom of the collector box as well as effect the development of secondary flow. For this scaled research, the ECB was built from SLS glass-filled nylon 12 material shown in Figure 4-2(b) above.

The annular diffuser was built from aluminum 6061 material with a special machined slot to hold the strut ring. The wetted area ratio of the diffuser exit to the strut ring inlet (A_2/A_1) is about 2. The axial length of diffusion with the strut ring installed is approximately 4 inches. The diffuser utilized two separate O-rings, one placed between the inlet face of the diffuser and the diffuser-collector flange and the other placed around the circumference of the diffuser to ensure an air tight seal between the diffuser and surrounding collector box.

4.1.1: Baseline Back-Wall and Hub

The back wall of the ECB was made from 3/8" thick clear acrylic material. The clear wall provided easy visibility for calibrating the radial traverse instrumentation and verifying the strut ring clocking. It consisted of a 4.916" diameter bore hole 1/8" deep to mate with the center body splash plate for a smooth flow transition between the hub and back wall. For instrumentation purpose, the back wall had 6 circumferential slots located every 60 degrees beginning at the 12 o'clock position to allow access to the hub pressure taps. In addition, the back wall also included 6 small access holes spaced every 60 degrees from one another that were staggered between the slots to allow for the internal hub pressure tubing. The back wall of the collector box is shown below in Figure 4-3(a).

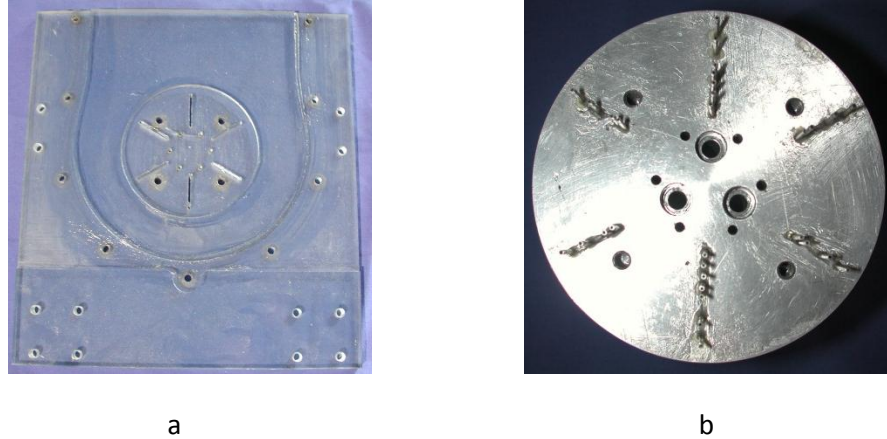


Figure 4-3: a) Back wall of the Collector Box Made From Clear Acrylic Material b) Front View of the Baseline Hub Showing the Various Static Pressure Ports.

The hub was constructed out of aluminum 6061 material incorporating the Solar Turbines near 45 degree splash plate. Several tunnels were drilled into the hub to provide pressure taps along the axial direction as seen in Figure 4-2(a). A total of 7 pressure taps were placed at the 0 and 180 degree locations with 4 of the taps positioned inside of the diffuser, 1 tap located in between the diffuser exit and splash plate, and the other 2 taps located on the splash plate. There were 4 pressure taps placed at the 60, 120, 240, and 300 locations responsible for measuring the static pressure from the exit of the diffuser to the extents of the splash plate. Finally, 6 - 9/64" diameter holes were drilled through the hub spaced 60 degrees apart from one another to support the 1/8" internal pressure tubing routed through the hub. This internal tubing was connected to the 6 static pressure taps located on the hub which lined up with the static taps on the case at the diffuser inlet plane. The flat surface of the hub with the installed static pressure taps is shown in Figure 4-3(b) above.

4.2 Baseline Geometry Results and Discussion

In an effort to design a more efficient diffuser-collector subsystem, the baseline model was experimentally tested and analyzed. Once certain flow phenomena were understood, the beneficial geometries could be reused while the detrimental geometries were improved upon creating a new, more efficient design.

4.2.1: Diffuser Inlet Conditions and Overall Subsystem Performance

The results of the baseline diffuser-collector configuration are listed below in

Table 4-1 and graphically depicted in Figure 4-4.

Table 4-1: Experimental Diffuser Inlet Performance Parameters with Overall Baseline Diffuser-Collector Geometry Performance Values.

	Baseline Diffuser-Collector
Average Inlet Conditions	
Mach Number, Ma	0.397
Static Pressure	13.001
Static Δ Pressure	-0.593
Total Pressure	14.495
Total Δ Pressure	0.900
Dynamic Pressure	1.495
Swirl, α , deg	7.0
Overall Performance	
Pressure Recovery, Cp	39.7%
Diffuser Performance	
Diffuser Pressure Recovery	52.3%
Collector Performance	
KEP_y	3.25
KEP_total	5.23

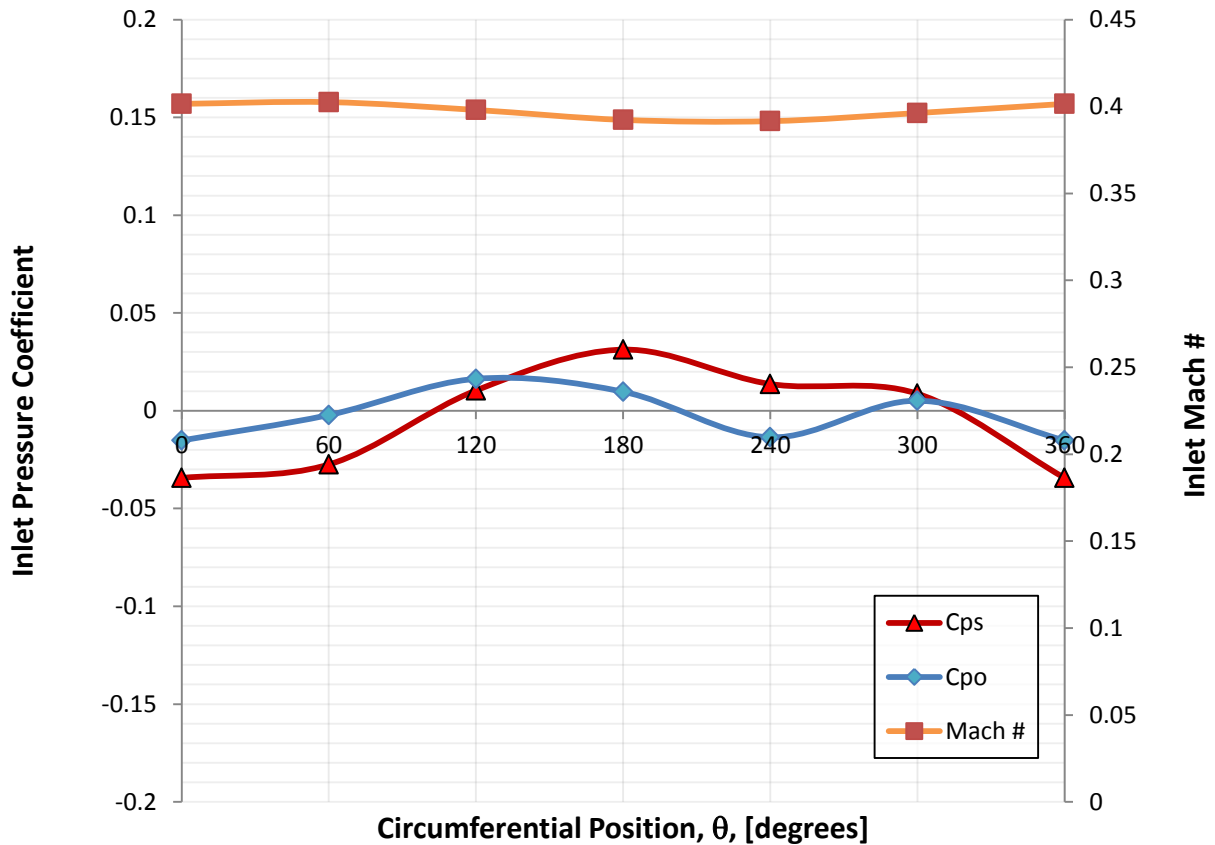


Figure 4-4: Circumferential Distribution of Inlet Total and Static Pressure Coefficients Along with Inlet Mach number.

The baseline diffuser-collector inlet data above shows that both the total and static pressure coefficient distributions are non-uniform. The static pressure coefficient distribution is near symmetric on either side of the 180° location while the total pressure coefficient distribution dips slightly at the 240° location. The high static pressure measured at the inlet of the diffuser at the 180° location is primarily due to the development of strong secondary flow within the small volume of the collector box comprised of the diffuser exit, collector bottom, pinch geometry, and back wall. A slight back pressuring effect of the diffuser can be seen from the static pressure profile due to the close proximity between the exit of the diffuser and the collector back wall. The Mach number shows an inverse trend to the static pressure in which a high static pressure yields a slower Mach number and vice versa, this is due to the flow taking the path of least resistance inside the diffuser. The overall subsystem pressure recovery of the baseline diffuser collector model was calculated to be 39.7%.

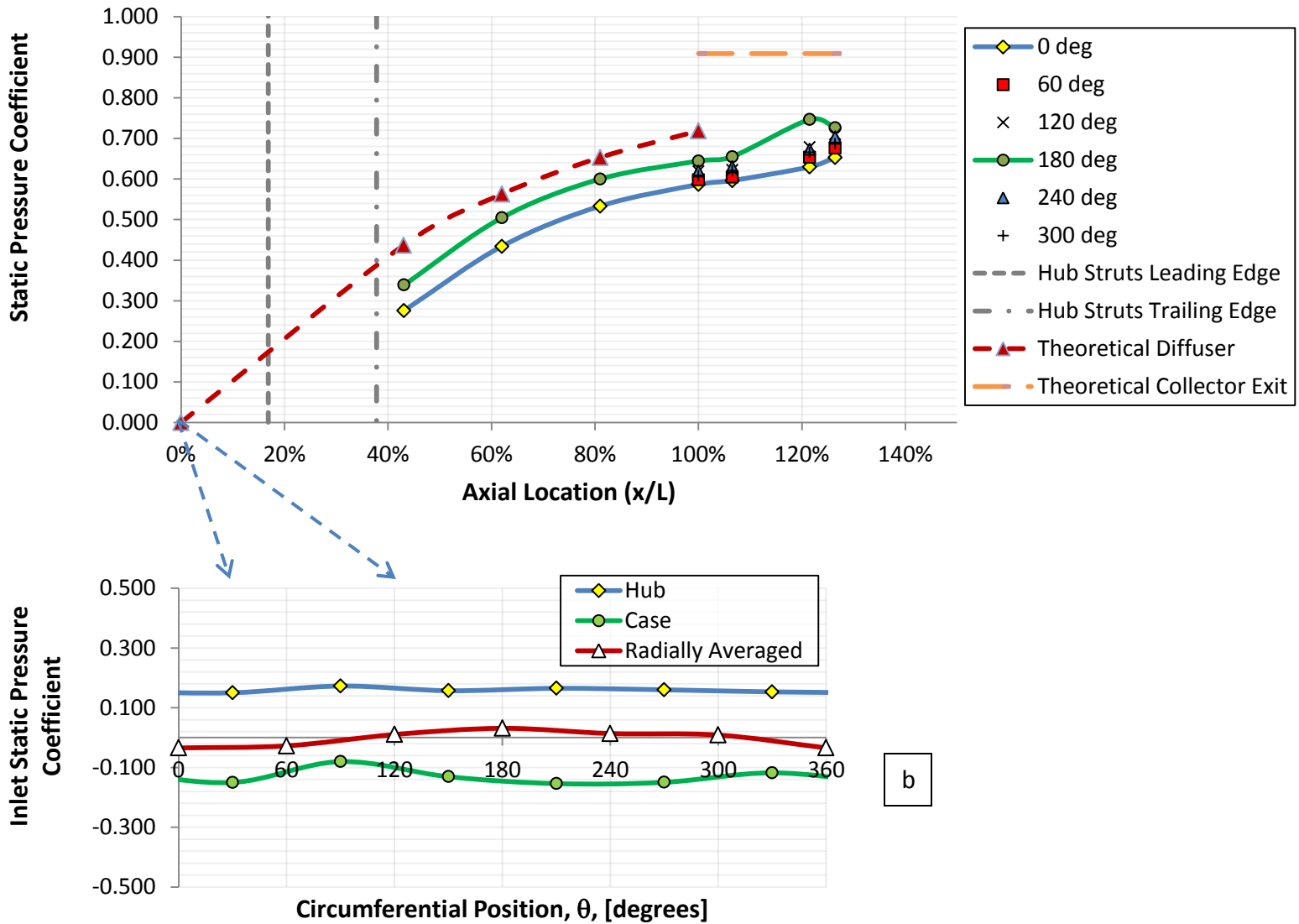


Figure 4-5: a) Static Pressure Profile in the Diffuser of the Baseline Diffuser-Collector Configuration. The Theoretical Static Pressure of the Diffuser and Collector are shown for Reference. b) Inlet Circumferential Pressure Distribution at $x/L = 0$ for the Diffuser as well as at the Case and Hub.

Figure 4-5(a) illustrates the static pressure rise occurring throughout the diffuser of the baseline configuration at the 0 and 180 degree circumferential locations as the fluid velocity is decreasing. Further detail of this well behaved diffuser flow is shown in section 4.2.3. Additional diffusion occurring outside of the shroud was measured using static pressure taps placed on the hub beginning from the exit of the diffuser ($x/L = 100\%$) to the extents of the centerbody splash plate ($x/L = 126\%$). The overall results show a continuous static pressure rise inside the diffuser to the centerbody splash plate at all of the measured circumferential locations besides at the $x/L = 126\%$ position of the 180 degree location where a small dip can be seen. The drop in static pressure is a sign of flow separation from the hub. The theoretical diffuser static pressure rise and the collector exit section static pressure are shown for reference and were calculated using Equation 4-1 based on area ratio. The theoretical static pressure at the exit of the collector has the largest value due to the large cross sectional area. The leading and trailing edges of the strut ring are denoted by the two different grey dashed lines on the plot.

Equation 4-1	$\frac{P_{s2} - P_{s1}}{\frac{\rho}{2} U_1^2} = 1 - \left(\frac{A_1}{A_2}\right)^2$
--------------	---

The diffuser Inlet measurements ($x/L = 0\%$) were taken using a combination of static pressure taps placed through the case and hub as well as a full circumferential-radial traverse described in section 3.2. The static pressures at the hub inlet were acquired utilizing internal pressure tubing routed inside of the hub as mentioned in section 4.1.1 Figure 4-5(b) verifies the presence of high pressure on the hub and low pressure on the case with the radially averaged annulus values in between. Furthermore, the upper (0°) annulus location is shown to have the lowest static pressure while the bottom of the annulus (180°) has the highest due to the back pressuring effect propagating to the diffuser inlet.

4.2.2 Collector Exit Section Data

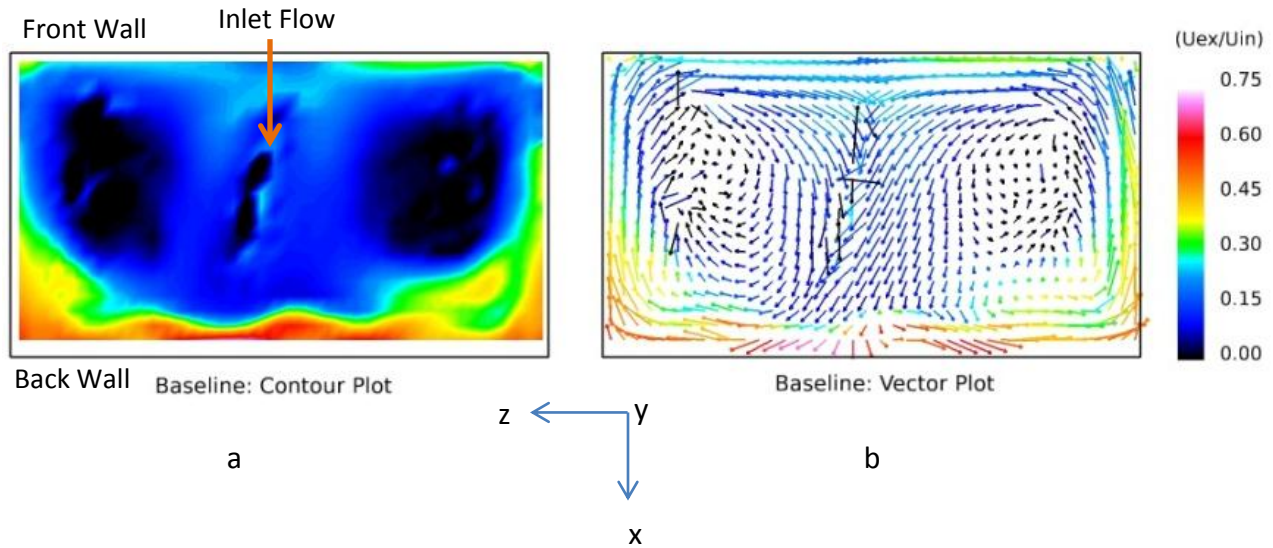


Figure 4-6: a) Contour Plot of the Radial Velocity Out of the Page (U_y) Within the Exit Section of the Baseline Diffuser-Collector Geometry. b) Flow Magnitude and Direction Shown by a Vector Plot of the Baseline Diffuser-Collector Geometry. The Collector Exit Velocity is Normalized by the Diffuser Inlet Velocity (U_{ex}/U_{in}).

Figure 4-6 was created by using data from the collector box exit traverse method explained in section Figure 3-3. It has been verified that two strong counter rotating vortices are formed within the exit section of the collector box shown in black in both of the figures above. These regions of slow or reversed flow are caused by the diffuser-collector subsystem geometry. As the axial flow exits the diffuser and impinges on the back wall of the collector in a nearly perpendicular manner, the high speed flow is forced to abruptly turn in all radial directions. By inducing this rapid turn in the flow, the two opposite rotating vortices are formed in the middle portion of the collector as shown by the vector plot above. The buildup of high momentum flow along the back wall is shown by the red color in the contour plot above. By essentially putting a flat plate at a small distance away from the exit of the diffuser, not only are the vortices formed within the collector box, but a back pressuring effect occurs within the diffuser. This propagation of pressure back into the diffuser causes flow separation and non-uniform pressure gradients at the exhaust of the LPT. With the presence of these low pressure vortices within the exit section of the collector box, the outflow is restricted and the total pressure loss of the subsystem is increased.

These areas of non-uniform flow within the exit section of the collector box prove detrimental to the overall subsystem pressure recovery and thus the efficiency of the gas turbine engine. The kinetic energy flux parameter of only the radial flow leaving the exit section of the collector box was found to be 3.25 while the total KEP was found to be 5.23. The specific geometries of

both the diffuser and the collector have a strong impact on the complex 3D flow structure formed within the collector box. These geometries must not be designed independently from one another, but rather together as a system. By utilizing this data from the baseline model, a new and more efficient diffuser-collector subsystem geometry was created.

4.2.3 Oil Flow Visualization

To gain a better understanding of the 3D surface flow streamlines within the baseline diffuser-collector configuration, surface oil flow visualization was performed shown in Figure 4-7 and Figure 4-8 below.

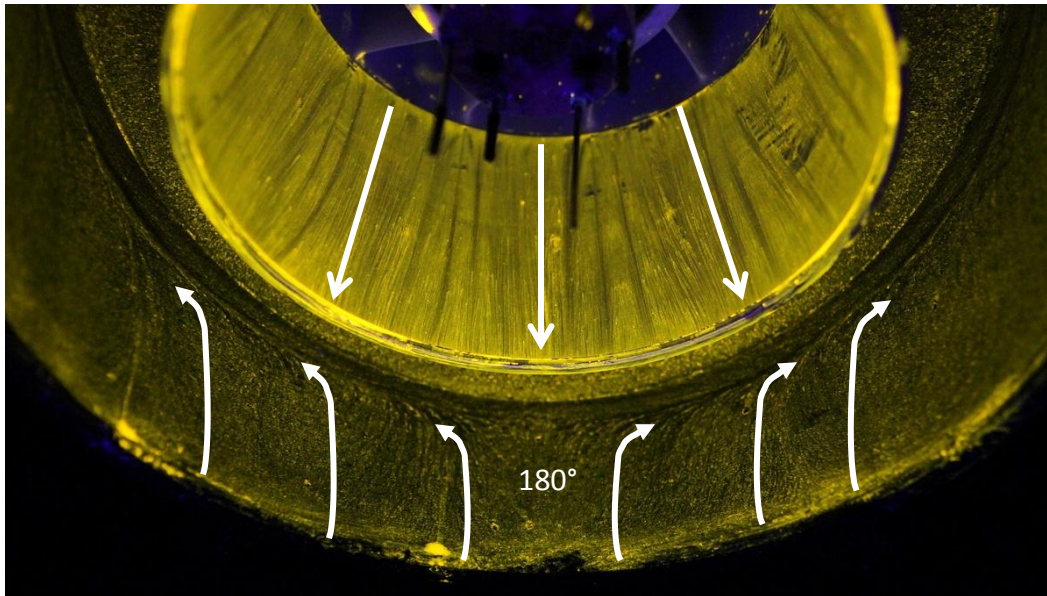


Figure 4-7: Surface Oil Flow Visualization in the Baseline Diffuser-Collector Configuration showing the Streamlines of the Diffuser and 180 Degree Portion of the Pinch Collector Box.

The baseline annular diffuser performed with very little flow separation on the inner shroud surface with the pinch collector box installed as shown by the exiting streamlines marked by the straight arrows. This oil flow visualization matches the result found in section 4.2.1 regarding a uniform static pressure rise throughout the diffuser. The effect of the impinging jet on the back wall of the pinch collector is shown by the split-reverse flow marked by the curved arrows at the bottom portion of the collector box.

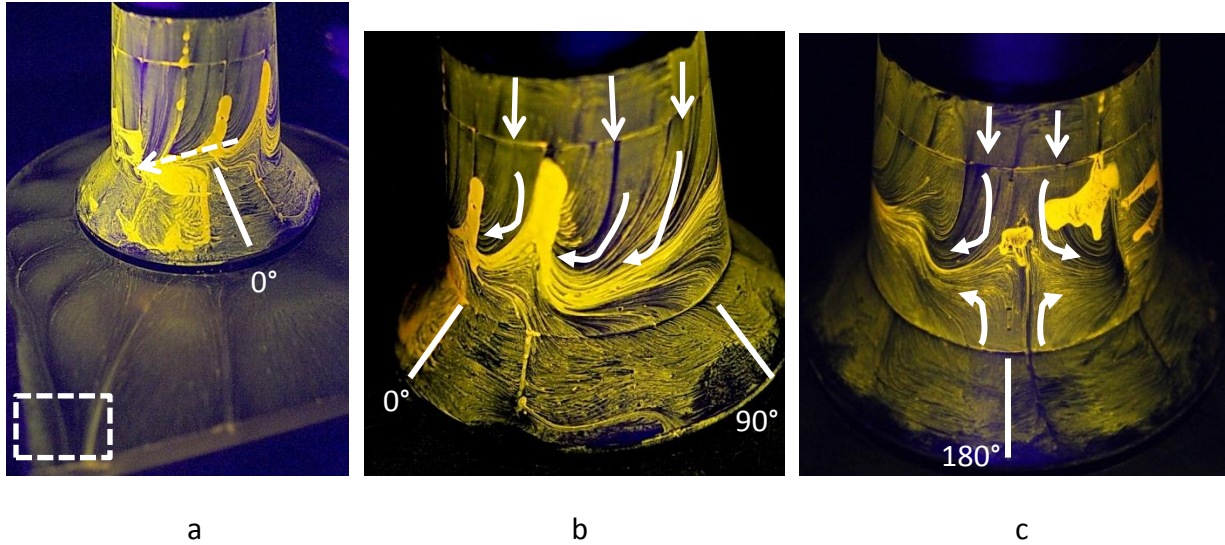


Figure 4-8: a) Streamlines on the Baseline Hub and Back wall. b) Close up of the Flow Reversal Streamlines on the Baseline Hub Between 0 to 90 Degrees. c) Separation Point on the Hub at the 180 Degree Location

As the flow expands within the diffuser and travels closer to the back wall, early separation on the hub is shown to be a large problem. Various separation regions were identified around the entire circumference of the hub with the majority of the reverse flow occurring before the diffuser exit. The areas of strong reverse flow are revealed by oil accumulation or pools on the hub. Figure 4-8(a) shows an early separation region around the 0° location with later separation occurring in the direction of the dotted arrow. Furthermore, axisymmetric lines formed by the strut wakes were identified on the back wall of the collector with a convergence near the corner as shown by the dashed box. Between 0 to 90 degrees, an area of strong reverse flow occurs as shown in Figure 4-8(b). At the 180° portion of the hub, slightly downstream of the struts, the flow began to split and quickly turn in the direction of the collector exit section (Figure 4-8(c)) caused by the presence of high static pressure and strong up-wash. These regions of separation and reverse flow on the hub cause deterioration in the diffuser pressure recovery thus must be greatly reduced in order to yield higher overall subsystem performance.

The baseline diffuser-collector design was improved by using various interchangeable geometries that fit within the existing packaging restraints. All geometries were varied only within the internal baseline collector box area. The interchangeable geometries were made from either aluminum 6061 or SLS glass filled-nylon 12 material. The SLS material was chosen for its quick turnaround time from concept to prototype as well as its temperature deflection properties of near 350 degrees Fahrenheit.

5.1: Flat Wall Collector Box Analysis

In this design, the pinch seen in the baseline ECB was removed, resulting in a vertical front wall and a larger overall volume within the collector. All other geometric dimensions and ECB materials were kept constant. The flat-wall collector box used the same back wall as the baseline model. The geometric difference between the baseline (pinch) and flat wall (non-pinch) can be seen in the figures below:

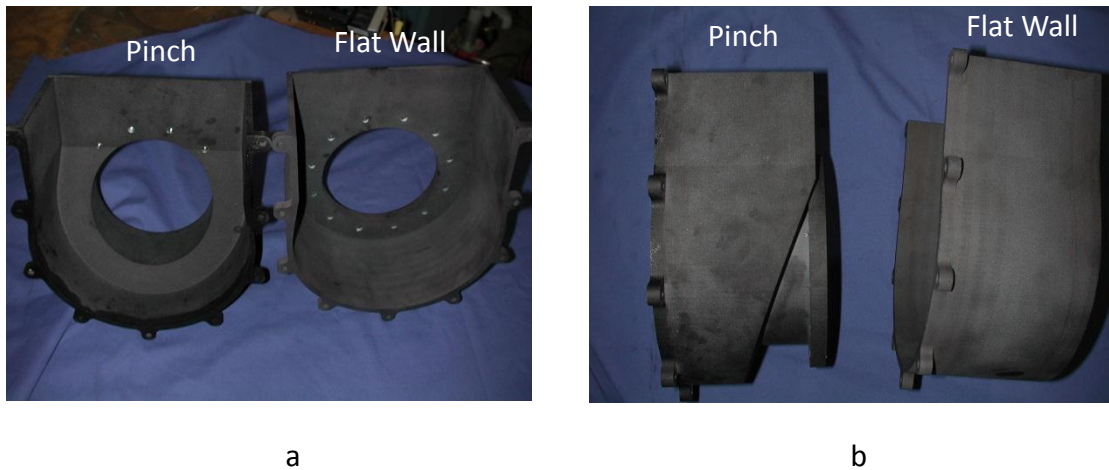


Figure 5-1: a) Rear View of the Baseline Pinch ECB (left) and Flat Wall ECB (right). b) Side View of the Baseline Pinch ECB (left) and Flat Wall ECB (right).

To understand the impact of the increased volume collector box without the pinch, all of the baseline components were reused except for the pinch ECB which was substituted for the flat wall ECB as shown in the comparison section views below.

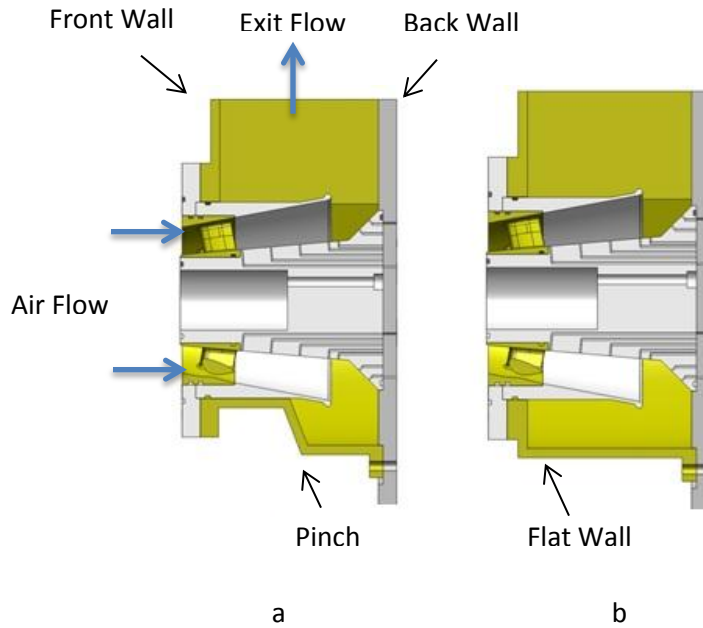


Figure 5-2: a) Section View of the Baseline Diffuser-Collector Geometry. Section View of the Baseline Components with the Flat Wall ECB Substituted. Figures are shown Side by Side for Comparison.

By incorporating this collector box substitution, the effect of the collector geometry on the overall subsystem performance could be studied. For every new geometry version, both the pinch and flat wall collectors were tested to determine which collector yielded the highest overall pressure recovery. The basis of this diffuser inlet analysis can be found in Appendix B.

5.1.1: Diffuser Inlet Parameters and Overall Subsystem Performance

Table 5-1: Inlet Performance Parameters and Overall Performance Values of the Flat Wall Collector Compared to the Baseline Pinch Collector

	Baseline Diffuser-Collector	Flat-Wall Collector w/Baseline Diffuser
<u>Average Inlet Conditions</u>		
Mach Number, Ma	0.397	0.402
Static Pressure	13.001	12.912
Static Δ Pressure	-0.593	-0.586
Total Pressure	14.495	14.430
Total Δ Pressure	0.900	0.931
Dynamic Pressure	1.495	1.518
Swirl, α , deg	7.0	7.4
<u>Overall Performance</u>		
Pressure Recovery, C_p	39.7%	38.6%
<u>Diffuser Performance</u>		
Diffuser Pressure Recovery	52.3%	52.0%
<u>Collector Performance</u>		
KEP_y	3.25	3.78
KEP_total	5.23	5.99

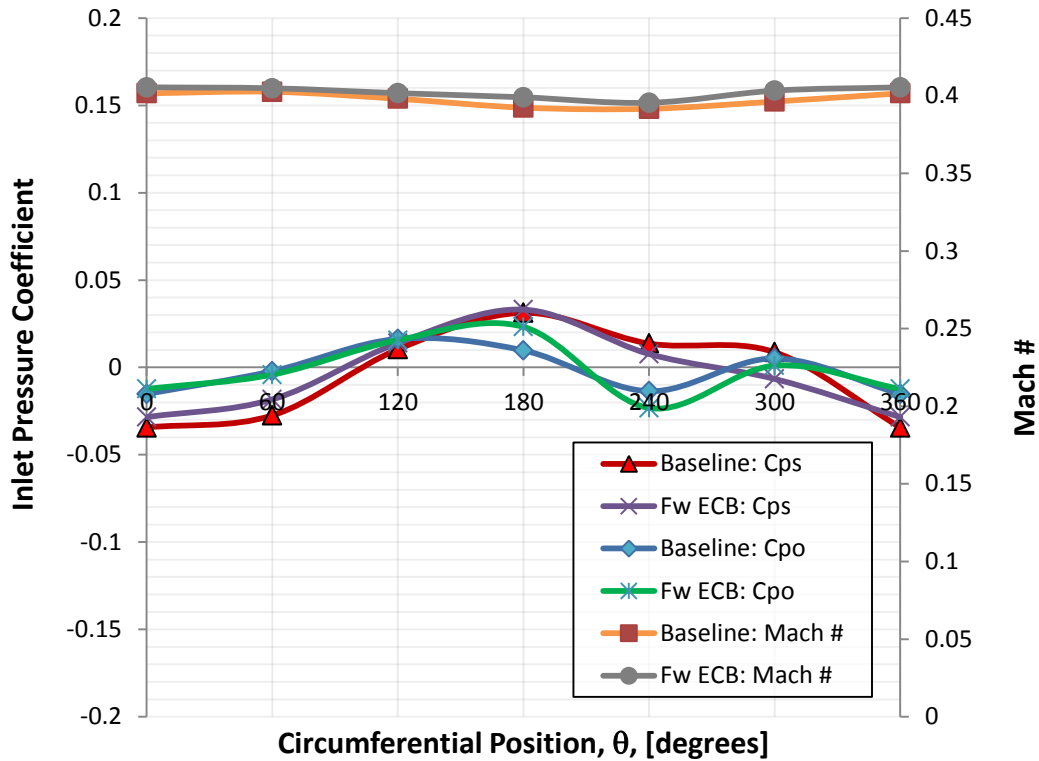


Figure 5-3: A Comparison of Baseline and Flat Wall Collector Geometry of the Circumferential Distribution of Inlet Total and Static Pressure Coefficients Along with Mach number.

The flat wall collector slightly raised the radially-circumferential average total and static pressures at the inlet of the baseline diffuser by 3.38% and 1.18% respectively. These numbers were based on differential pressure values so as to not skew the results due to fluctuations in atmospheric pressure. This pressure rise at the diffuser inlet was primarily due to the decrease in kinetic energy conversion throughout the diffuser, thus caused a decrease in diffuser pressure recovery by 0.3%. The inlet Mach number was shown to relatively increase at all circumferential positions as shown in Figure 5-3 above.

5.1.2: Collector Exit Section Data

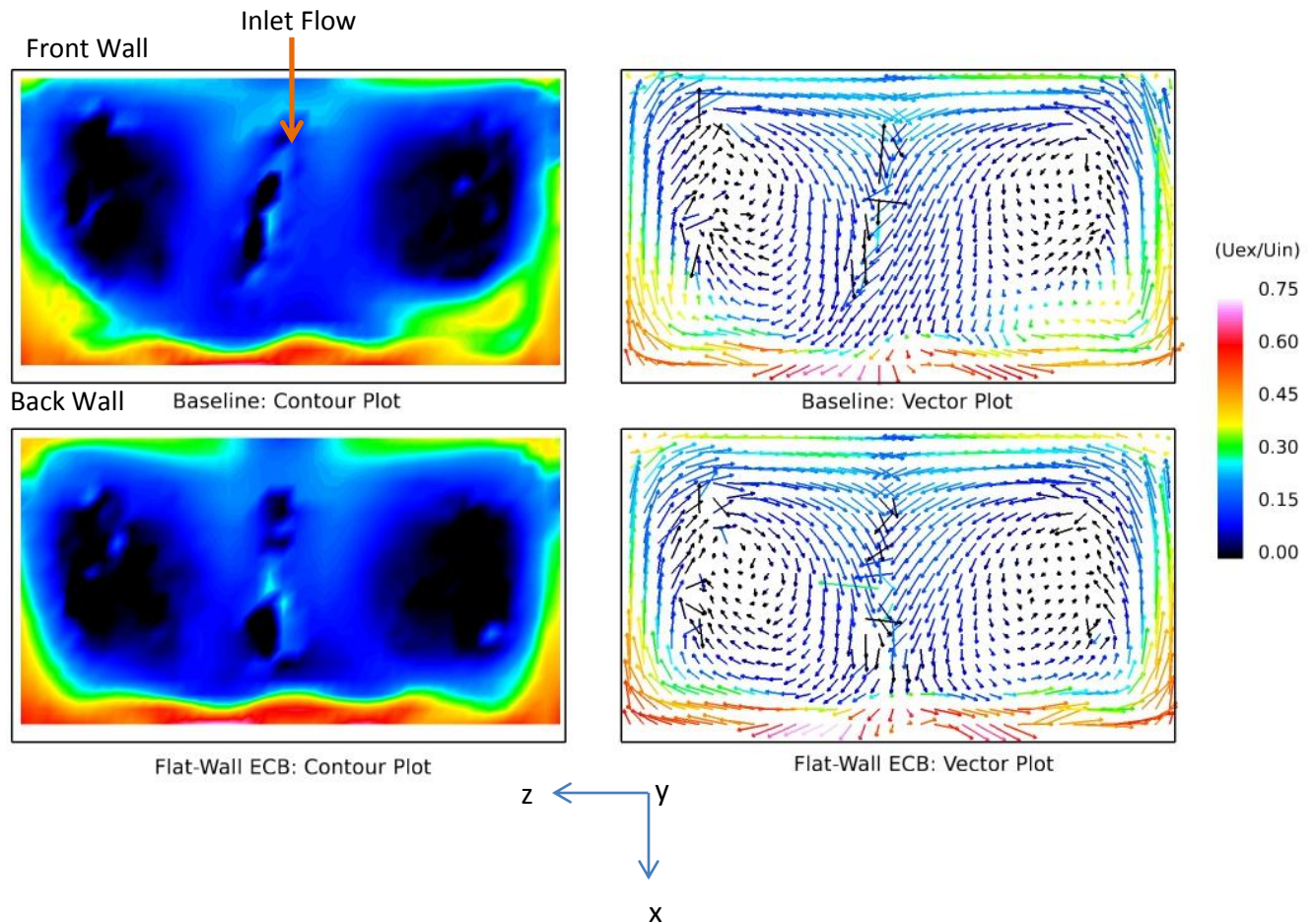


Figure 5-4: A comparison of Exit Contour and Vector Plots Between the Baseline Diffuser-Collector Geometry (left) and the Substituted Flat Wall ECB Geometry (right). The Collector Exit Velocity is Normalized by the Diffuser Inlet Velocity.

The exit contour plots in figure 5-4 above illustrate that the flat wall collector box generated a greater region of slow radial exit flow with the absence of the pinch as shown by the additional blue color near the back wall half of the collector. The high loss cores shown in black seem to remain the same due to similar axial flow impingement on the back wall. The flat wall ECB geometry did however generate more exit flow against the +Z front wall due to the vertical front wall surface shown by an increase in green area in the contour plot. Overall, the flat wall collector geometry produced a more non-uniform flow out of the collector exit section by rising the KEP radial value by 0.53 and the increasing the KEP total value from 5.23 to 5.99. Although the flat wall geometry was found to have an overall worse pressure recovery by 1.1% when

using the baseline components, this study will further prove that the flat wall collector is beneficial after introducing additional interchangeable geometries.

5.2: Tilted Diffuser-Flat Wall Collector Analysis

In an effort to suppress both the secondary flow inside the collector box and the strong axial jet up against the back wall, a diffuser was designed to allow the flow to expand while also translating upward towards the exit section of the collector box. This design was sought to create a more uniform circumferential pressure recovery compared to a conventional straight (non-tilted) diffuser [(Hardin, 2010)].

For this study, 3 different tilted diffuser angles including the existing 0 degree (non-tilt) baseline model were designed and experimentally tested for a total of 4 angle variations; 0, 5, 7, and 9 degrees. The tilt of the diffuser began directly downstream of the strut ring and was referenced by the common horizontal centerline as shown below in Figure 5-5(a). Since the diffuser was no longer an axisymmetric body of revolution, the loft feature in the Computer Aided Design (CAD) software, Solidworks was utilized. This meant that SLS rapid prototyping was essential for manufacturing. It's shown in Figure 5-5(a) with the center body positioned in its normal axial location perpendicular with the back wall, as the tilt angle of the diffuser increased, the outflow area at the 0 degree location increased while the outflow area at the 180 degree location decreased.

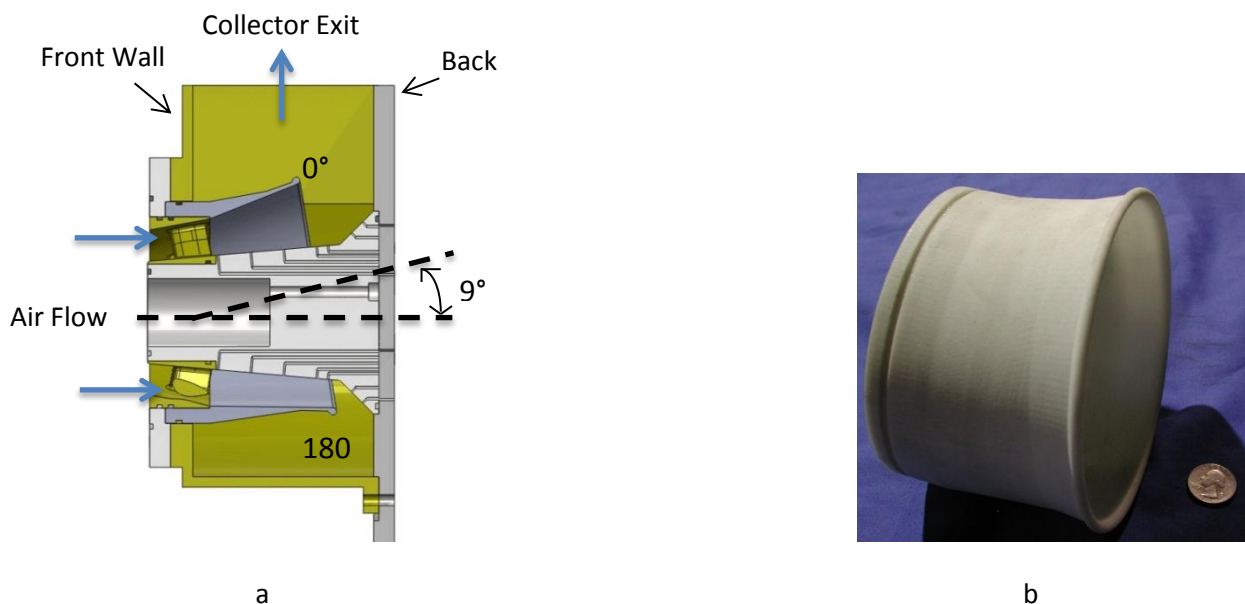


Figure 5-5: a) Section View of the 9 Degree Tilted Diffuser with Flat Wall Collector. b) Experimental 9 Degree SLS Tilted Diffuser Shown to Scale by a Quarter.

5.2.1: Diffuser Inlet Parameters and Overall Subsystem Performance

As mentioned in section 5.2 above, a total of 4 different diffuser tilt angles (including baseline 0 degree tilt) were experimentally analyzed. The flat-wall collector box was determined to yield a higher overall system pressure recovery compared to the pinch collector box while using a tilted diffuser design. The basis of this time-efficient, accurate test is explained in Appendix B.

A summary performance table is listed below displaying each of the 4 titled angles incorporating the flat wall collector along with the baseline diffuser-collector box for comparison. A plot of overall pressure recovery and total KEP versus diffuser tilt angle is also provided for performance trend analysis. The diffuser pressure recovery values that are shown were obtained by using the axial positioned pressure taps instrumented within the hub while the collector was installed. The tilt provided a non-axisymmetric diffuser, thus the center body taps could no longer be used in the diffuser pressure recovery calculations.

Table 5-2: Tilted Diffuser Performance Table with Flat Wall Collector Showing Experimental Inlet Run Conditions, Pressure Recoveries, and KEP Values.

	Baseline Diffuser-Collector	Flat-Wall Collector w/Baseline Diffuser	Flat-Wall Collector w/5 Deg Tilted Diffuser	Flat-Wall Collector w/7 Deg Tilted Diffuser	Flat-Wall Collector w/9 Deg Tilted Diffuser
<u>Average Inlet Conditions</u>					
Mach Number, Ma	0.397	0.402	0.400	0.402	0.401
Static Pressure	13.001	12.912	12.995	12.941	13.003
Static Δ Pressure	-0.593	-0.586	-0.673	-0.685	-0.685
Total Pressure	14.495	14.430	14.510	14.462	14.527
Total Δ Pressure	0.900	0.931	0.834	0.837	0.836
Dynamic Pressure	1.495	1.518	1.515	1.520	1.524
Swirl, α , deg	7.0	7.4	6.3	6.8	6.9
<u>Overall Performance</u>					
Pressure Recovery, C_p	39.7%	38.6%	44.6%	45.0%	45.0%
<u>Diffuser Performance</u>					
Diffuser Pressure Recovery	52.3%	52.0%	NA	NA	NA
<u>Collector Performance</u>					
KEP _y	3.25	3.78	3.08	2.82	2.82
KEP _{total}	5.23	5.99	4.90	4.57	4.51

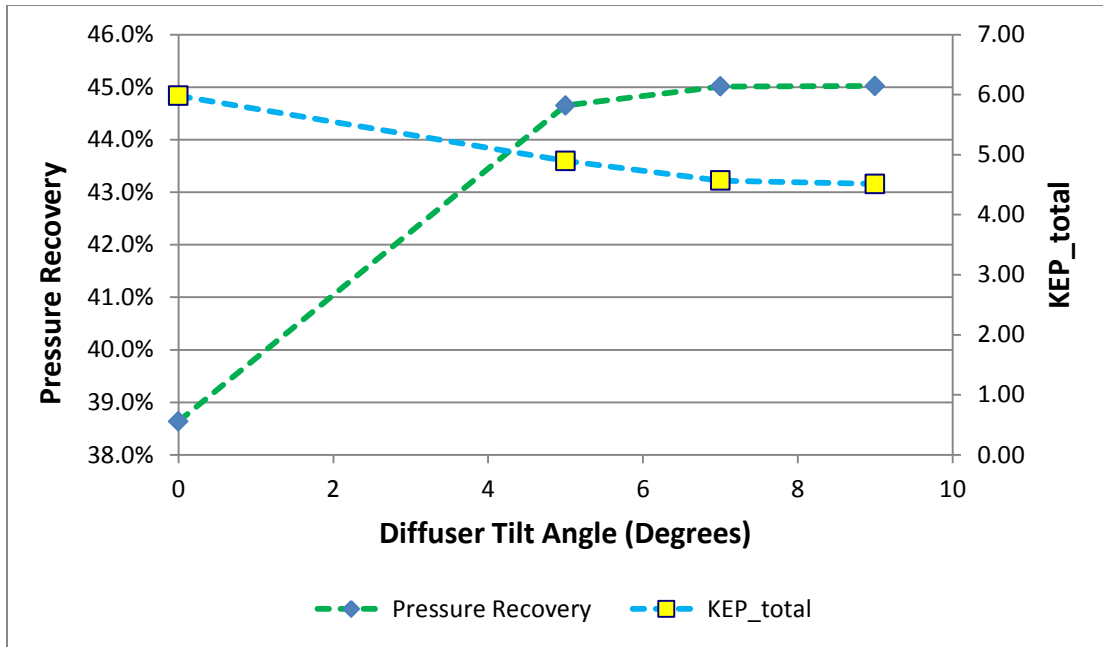


Figure 5-6: Tilted Diffuser Analysis of Overall System Pressure Recovery and Total KEP vs. Diffuser Tilt Angle

As shown from the tilted diffuser parametric study, by utilizing a tilted diffuser design and flat wall collector, the overall system pressure recovery and total KEP values were improved compared to the baseline diffuser collector. The improvement in pressure recovery occurred due to the decrease in both the differential static and total pressures at the inlet of the diffuser. The overall system pressure recovery was increased by 5.3% from baseline and the KEP total value was brought down from 5.23 to 4.51 with the 9 degree tilted diffuser. The trend shows that as the tilt angle of the diffuser increases, the pressure recovery also increases and the KEP value decreases. This trend holds true until the diffuser tilt angle reaches above 7 degrees, once this occurs the pressure recovery and KEP values begin to plateau signifying the maximum possible performance improvement with this specific geometry. These values are indicated in Table 5-2.

Even though the above improvements were seen, the static pressure gradients at the inlet of the diffuser also known as the exit of the low pressure turbine (LPT) needed to be studied. The graph below illustrates the effect of the diffuser tilt angle and flat wall collector on the inlet static pressure by showing the circumferential inlet static pressure coefficient distribution.

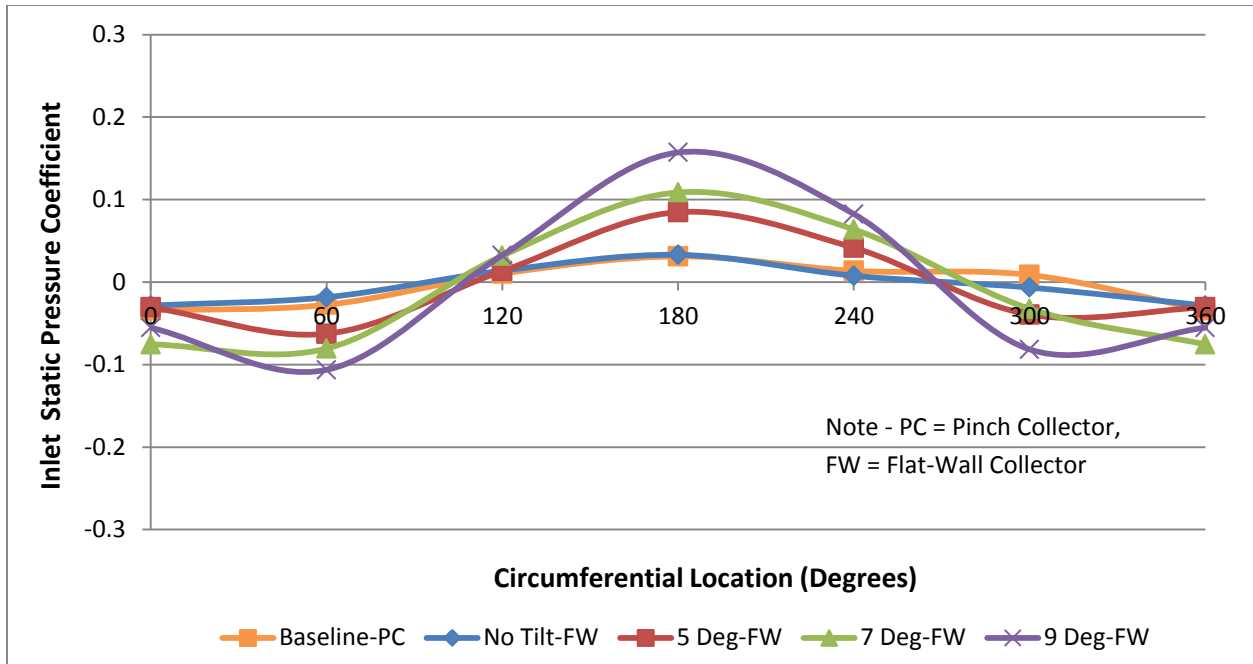


Figure 5-7: Inlet Static Pressure Coefficient Distribution for Tilted Diffusers with Flat Wall Collector Box. The Baseline Diffuser-Collector Subsystem is shown for Reference in Orange.

The figure above shows that as the tilt angle of the diffuser increases within the flat wall collector box, the non-uniform circumferential static pressure coefficient distribution at the inlet of the diffuser proportionally increases. A greater static pressure rise at the 180 degree location can be seen from each increasing tilt angle due to the flow area restriction of pinching the flow between the exit of the diffuser and the baseline splash plate/back wall. There is a trade-off present between overall subsystem pressure recovery and the static pressure distortions after the last blade row of the LPT.

5.2.2: Collector Exit Section Data

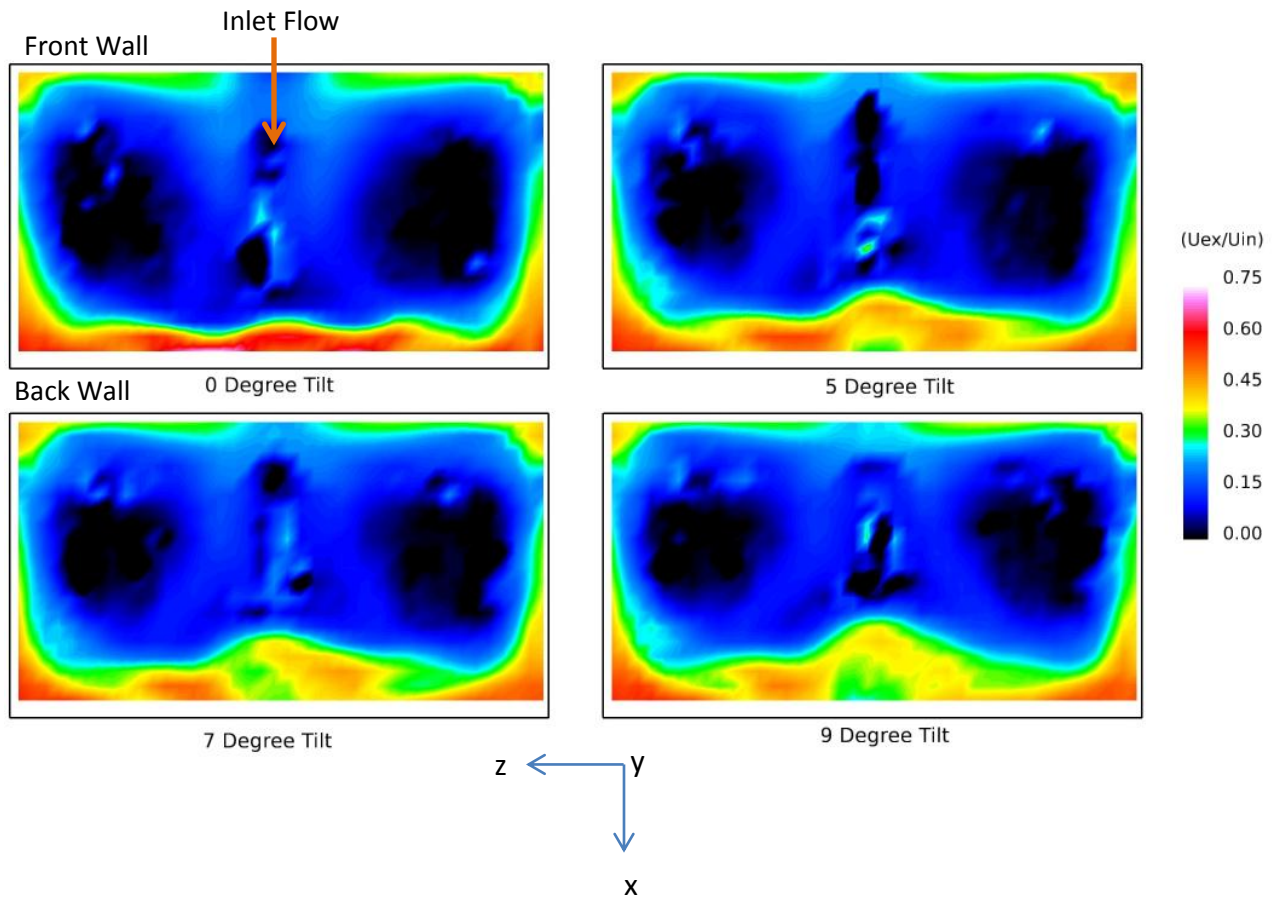


Figure 5-8: Contour Plots Showing the Normalized Exit Velocity of the 4 Different Diffuser Tilt Angles within the Flat Wall Collector Box. Exit Flow is Leaving the Page.

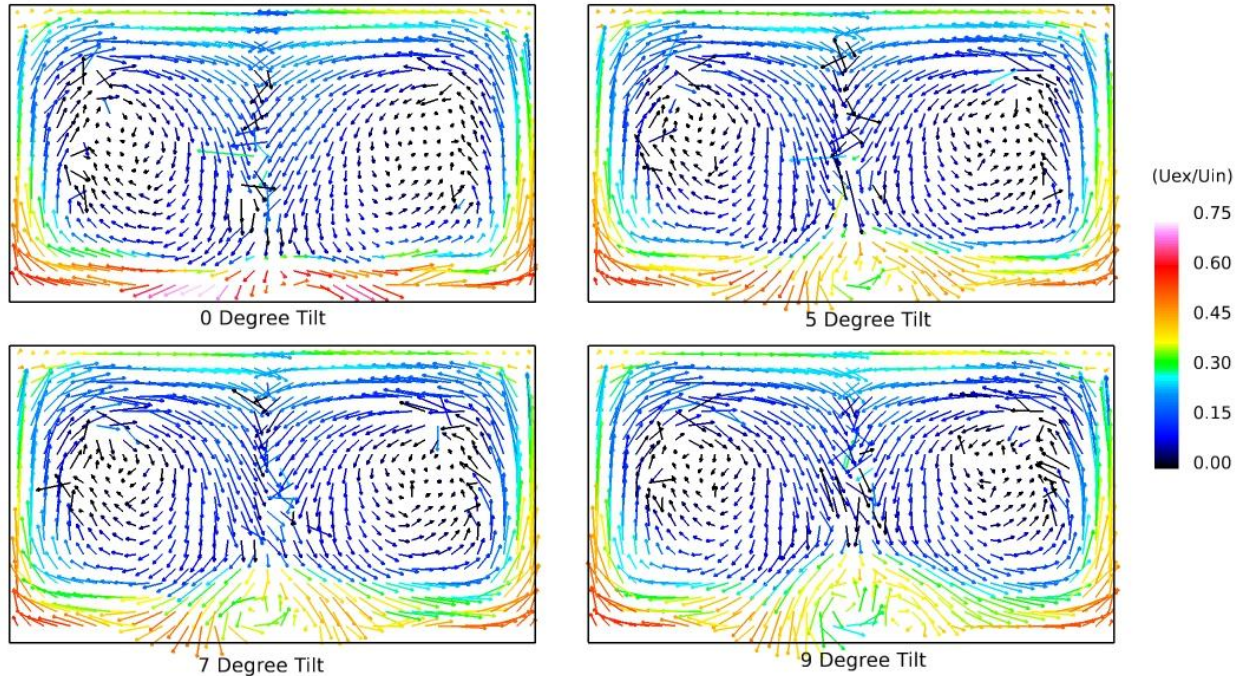


Figure 5-9: A Normalized Vector Plot comparison of the 4 Diffuser Tilt Angles Within the Flat Wall Collector Box.

The collector box exit section data above was taken using the exit traverse setup found in Figure 3-3(b). The baseline diffuser (0 degree tilt) contour plot (top left) shows a strong axial impinging jet up against the back wall of the collector. This exit jet is represented by the dark red color on the velocity scale and contributes to a non-uniform exit velocity and high KEP collector outflow. By increasing the diffuser tilt angle toward the exit section of the collector, the high radial velocity against the back wall is diminished and spread into the collector creating a more uniform outflow. This trend can be seen throughout each increasing tilt angle contour plot by noticing the green curve like shape growing in size away from the back wall and into the collector exit area shown in Figure 5-8. Furthermore, the high loss cores in the middle portion of the collector box were shown to slightly decrease in strength and size. As the diffuser tilts more towards the exit section (increased angle) the impinging jet on the back wall is less perpendicular. This effectively reduces the strength of the radial outflow on the back wall generating less circular momentum to support the low pressure regions. The magnitude and directions of the diffuser exit flow impinging on the back wall is shown in Figure 5-9.

5.3: Radial Diffuser-Pinch Collector Analysis

A parametric study was performed on a radial diffuser by varying the diffuser shroud radii to achieve the best overall subsystem pressure recovery within the pinch ECB. Both collectors were experimentally tested with each radial geometry using the inlet technique found in Appendix B. The smaller radii diffusers were found to perform better within the pinch collector, while the large radii diffusers preferred the flat wall collector. All radial geometries were tested using the pinch collector to understand the effects of only changing a single parameter. The radial diffuser design was created to allow the flow to expand within a larger area, thus increase the pressure recovery of the diffuser. Furthermore, the flow began smoothly transitioning from the axial to radial direction sooner compared to the previous designs.

Four different radial diffusers were selected for the basis of this research with radius to exit height ratios of 0.25, 0.5, 0.75 and 1.0. The radius (r) to exit height (h) (r/h) ratios were normalized by using the height from the exit of the baseline diffuser to the center body hub known as 1.143". This definition can be seen in Figure 5-10 below:

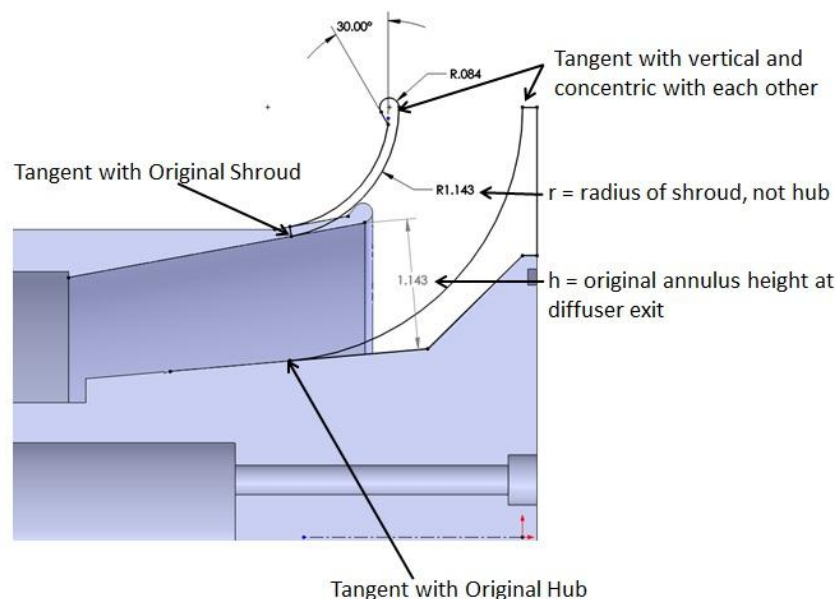


Figure 5-10: Zoomed in Section View of the Baseline Diffuser-Hub Showing the Exit Height of 1.143" known as (h) and the Radius of the Diffuser Shroud (r) for Calculating Radial Hardware Ratios (r/h).

In order to experimentally test various radial diffusers, several new components had to be designed to work with the existing small scale facility as shown in Figure 5-11 below. Each radial diffuser (shown in green below) required its own hub of equal radius (shown in purple). The hub radius was constructed such that once it was vertically tangent with the back wall, the hub continued expanding radially outward with a constant thickness of 1/8". The hubs were manufactured from 6061 aluminum each having the same axial length as the other and

included an O-ring groove on the face of the radial hub to form a tight seal with the back wall. By using the same axial length for each hub, only one new back wall needed to be created to support all radial diffuser tests. The back wall (shown in turquoise) was made from 3/8" thick 6061 aluminum having a borehole diameter of 7.75" and 1/8" deep to support a flush mount between the radial hub and back wall.

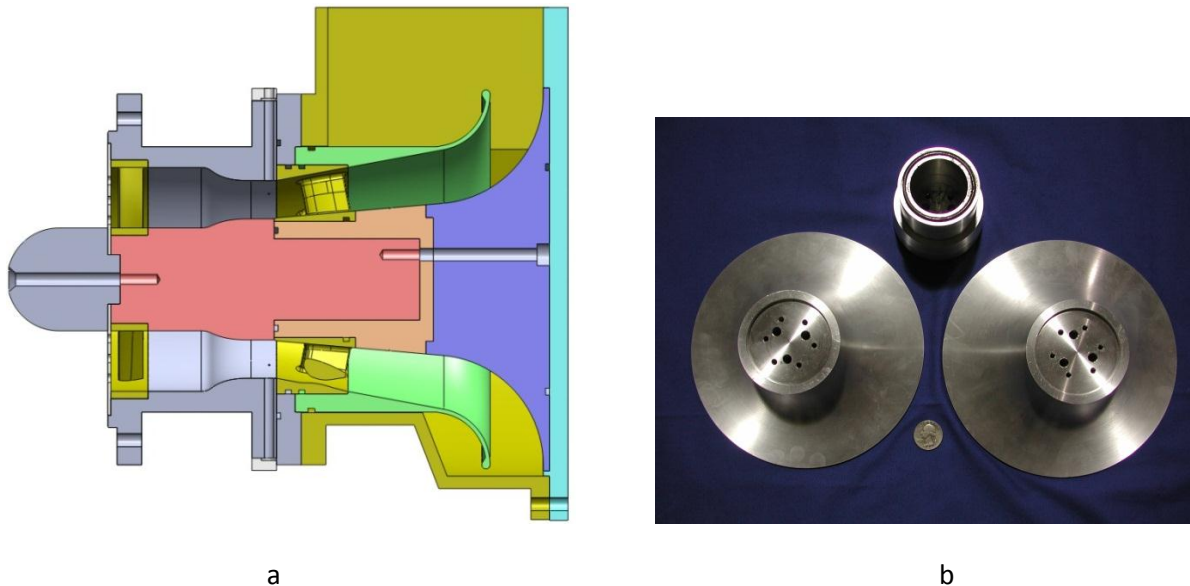


Figure 5-11: a) Section View of the $r/h=1.0$ Radial Diffuser Hardware Components. b) Radial Hubs and Adapter Piece with O-ring shown to Scale by a Quarter.

In addition to a new back wall, an adapter piece (shown in orange) was created that joined the existing center body (shown in red) to the radial hubs. The adapter was made from the same 6061 aluminum material and was manufactured with an O-ring groove for a tight circumferential seal with the existing center body shaft.

5.3.1: Diffuser Inlet Parameters and Overall Subsystem Performance

Below is the performance table showing the 4 different radial diffuser hardware designs along with the baseline diffuser collector configuration for comparison purpose. The diffuser pressure recovery values were obtained by experimentally testing each diffuser without the collector box installed. The methodology of these diffuser only tests is outlined in section 5.5.

Table 5-3: Radial Diffuser Hardware Design Performance Table with Pinch Collector Showing Experimental Inlet Run Conditions, Pressure Recoveries, and KEP Values.

	Baseline Diffuser-Collector	Pinch Collector w/ r/h=0.25 Radial Diffuser	Pinch Collector w/ r/h=0.5 Radial Diffuser	Pinch Collector w/ r/h=0.75 Radial Diffuser	Pinch Collector w/ r/h=1.0 Radial Diffuser
<u>Average Inlet Conditions</u>					
Mach Number, Ma	0.397	0.404	0.409	0.405	0.399
Static Pressure	13.001	12.906	12.870	12.910	13.153
Static Δ Pressure	-0.593	-0.647	-0.736	-0.688	-0.536
Total Pressure	14.495	14.441	14.438	14.456	14.681
Total Δ Pressure	0.900	0.887	0.838	0.856	0.992
Dynamic Pressure	1.495	1.535	1.567	1.546	1.529
Swirl, α , deg	7.0	6.6	6.8	6.5	6.8
<u>Overall Performance</u>					
Pressure Recovery, Cp	39.7%	42.2%	46.7%	44.5%	35.1%
<u>Diffuser Performance</u>					
Diffuser Pressure Recovery	52.0%	42.3%	48.8%	51.3%	52.9%
<u>Collector Performance</u>					
KEP _y	3.25	2.89	2.80	3.75	4.84
KEP _{total}	5.23	4.86	4.43	5.56	6.56

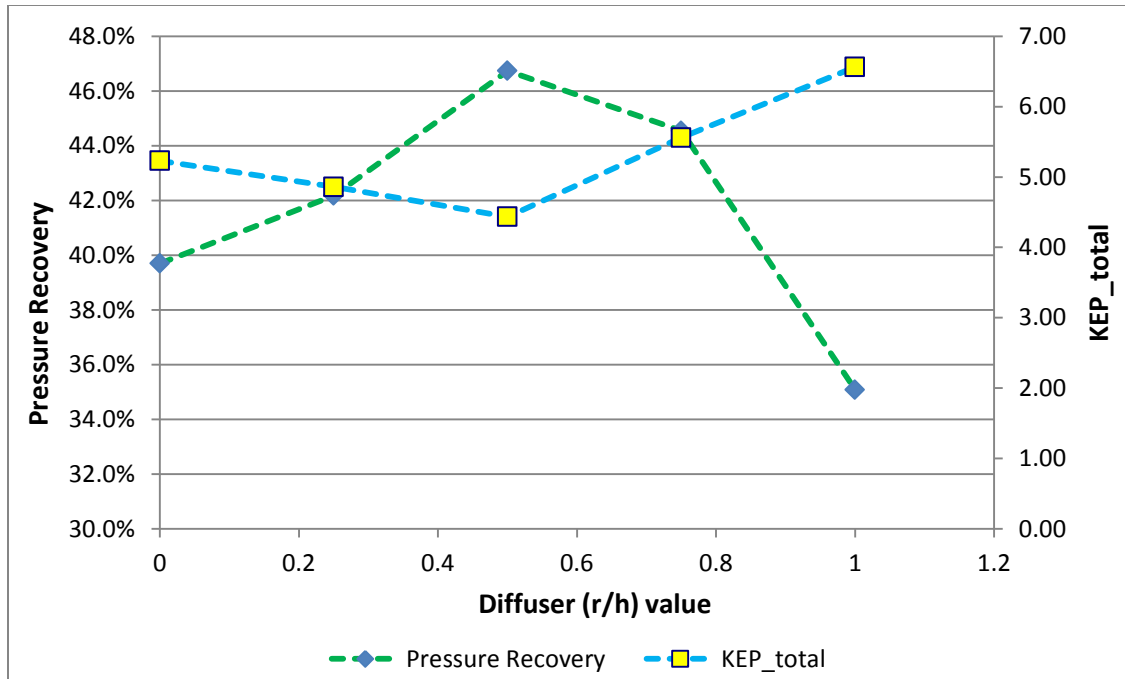


Figure 5-12: Radial Diffuser Hardware with Pinch Collector Analysis of Overall System Pressure Recovery and Total KEP vs. Diffuser r/h value. The r/h Value of Zero Represents the Baseline Case.

The results above illustrate that an inverse trend is present between overall pressure recovery and total KEP values. As the diffuser r/h value increases from baseline (0), the pressure recovery of the system increases while the KEP value decreases. This signifies that both the r/h=0.25 and r/h=0.5 radial diffusers were successful in further expanding the flow within the larger cross-sectional area, thus converting more of the kinetic energy at the inlet of the diffuser into a pressure rise compared to the baseline configuration. As a result, the inlet total pressure was reduced, providing a larger expansion ratio across the LPT. This trend is valid until after the r/h=0.5 case in which the radial diffuser becomes large enough to begin negatively impacting the performance of the diffuser-collector system. Early flow separation was found to occur inside the large r/h=1.0 radial diffuser which negatively impacted its diffuser efficiency and drastically decreased the overall pressure recovery as shown in Figure 5-12. This parametric study confirmed that the best radial diffuser hardware design was found at an r/h value of 0.5 having an overall pressure recovery of 46.7% and a total KEP value of 4.43.

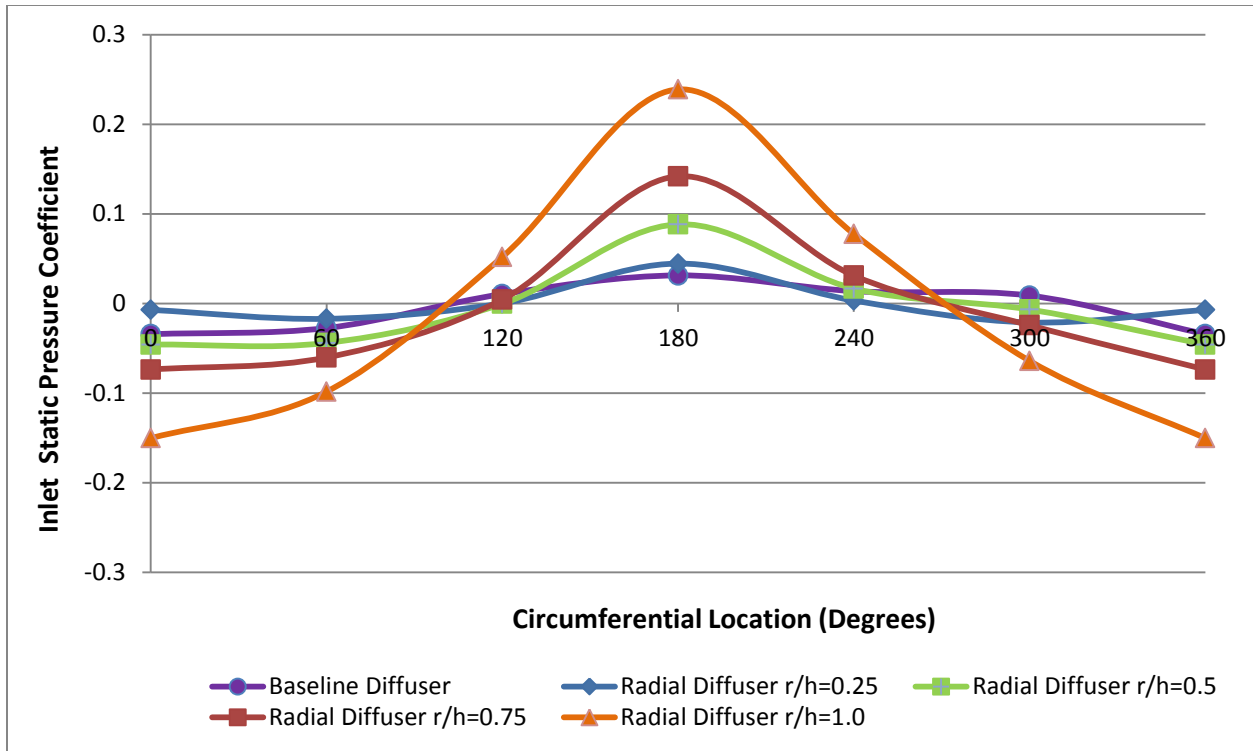


Figure 5-13: Inlet Static Pressure Coefficient Distribution for Radial Hardware Designs with Pinch Collector Box. The Baseline Diffuser Collector Subsystem is shown for Reference.

The chart above reveals that as the r/h value increases, the inlet static pressure coefficient has a more non-uniform circumferential distribution. The greatest static pressure rise can be seen at the 180 degree location, growing in size as the diffuser radii increases. Due to the geometry of the radial diffuser inside the pinched collector box, a larger wall begins to form with each increase in r/h value closing the gap between the exit of the diffuser and the bottom portion of the collector box. With the presence of this radial diffuser wall and the decrease in distance between the diffuser exit and back wall, the flow exiting the diffuser can no longer expand within the entire collector box. This essentially back pressures the diffuser causing the static pressure rise as shown and generates a large region of secondary flow in the bottom portion of the collector.

5.3.2: Collector Exit Section Data

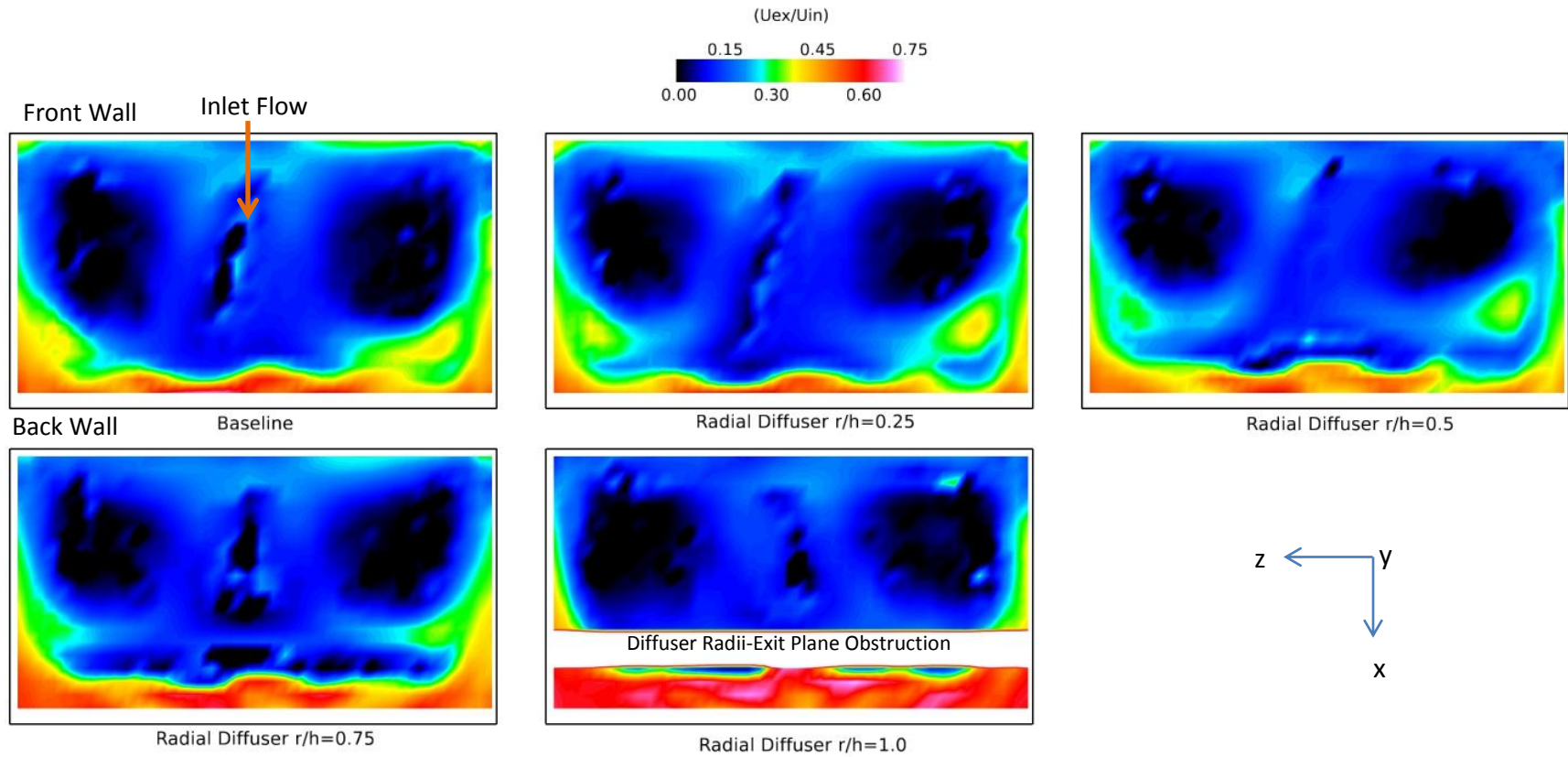


Figure 5-14: Contour Plots Showing the Exit Velocity of the 4 Different r/h Radial Diffuser Hardware Designs within the Pinch Collector Box. The Baseline Diffuser Collector Box is also shown for Comparison. Flow Exiting the Collector Box is Out of the Page.

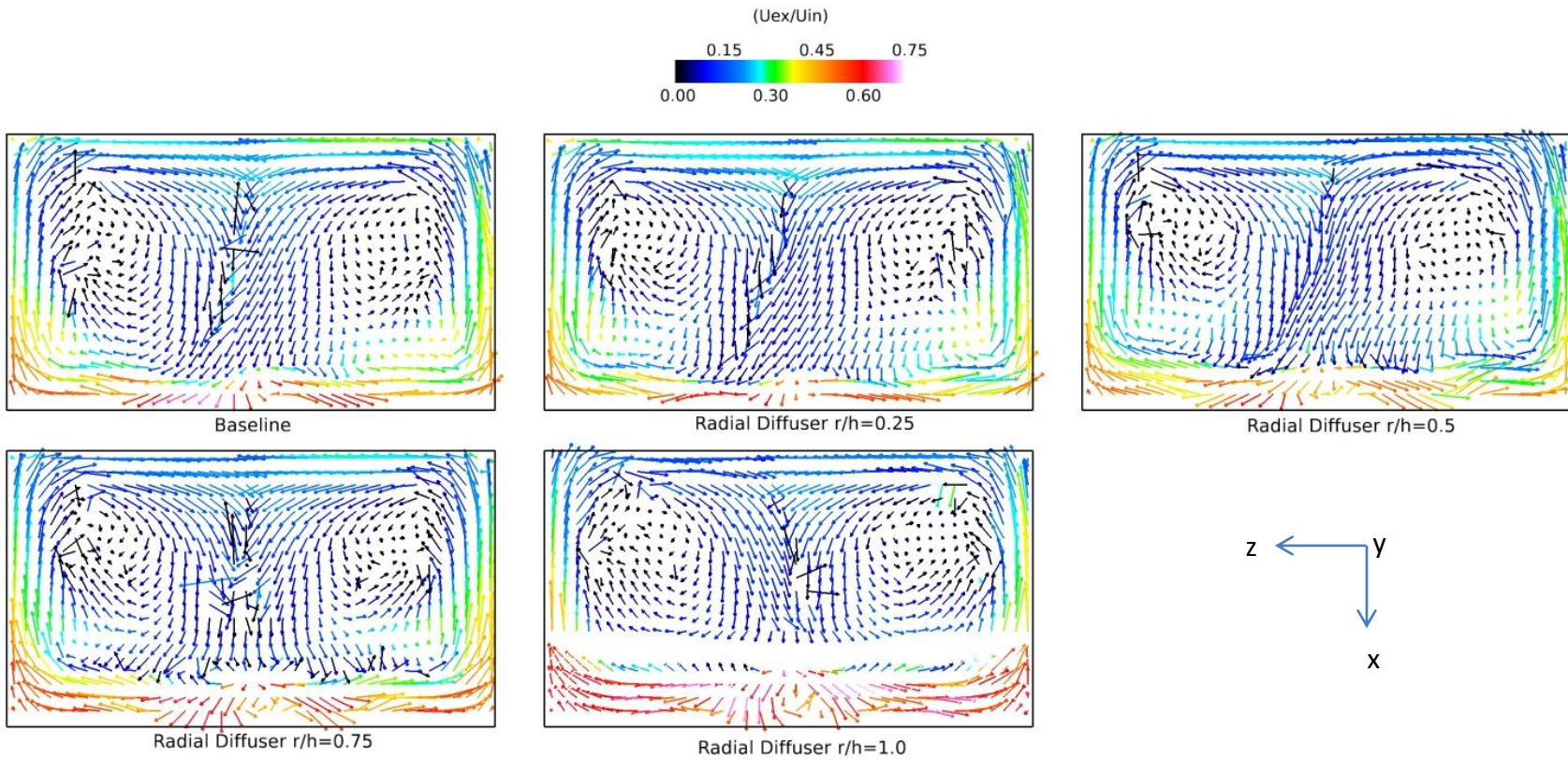


Figure 5-15: Normalized Vector Plot of the Radial Diffusers. Baseline Geometry Included for Reference.

The collector exit traverse plots above illustrate the effects of the radial diffuser within the pinch collector box. As the radial diffuser increases in size, a strong radial jet begins to form on the back wall of the collector as shown by the red and white colors. This jet increases in strength due to the radii increase of the diffuser getting closer to the back wall. Flow leaving the diffuser continues in its radial direction longer with a greater r/h value, but without expanding within the area of the collector. Another phenomenon can be seen from these side by side comparisons, in which the upward velocity against the front wall decreases as the r/h value is increased shown by the slower dark blue color. This occurs due to the wall like formation of increasing the r/h value of the radial diffuser creating a barrier between the flow exiting the diffuser and the bottom portion of the collector box. A blockage like this generates detrimental performance values as shown by the $r/h=1.0$ radial diffuser with an overall pressure recovery of 35.1% and a large KEP value of 6.56.

5.3.3 Oil Flow Visualization

The images shown in this section are with the $r/h=1.0$ radial diffuser inside the slightly better performing flat wall collector box. The primary reason for this change in collector is explained in section 5.4.

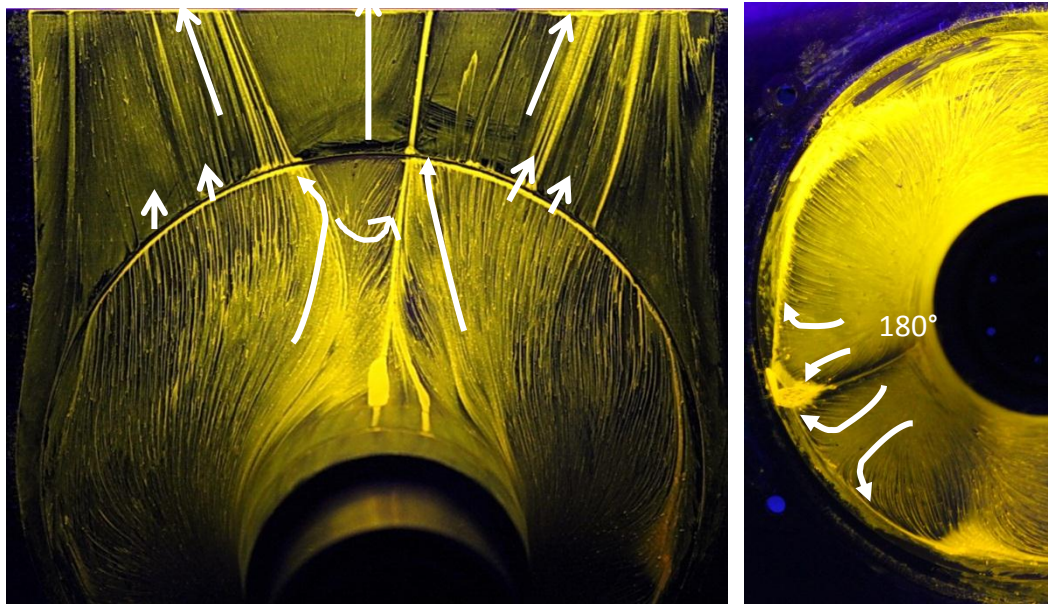


Figure 5-16: a) Surface Oil Flow Visualization of the $r/h=1.0$ Radial Hub and Back Wall. b) Separation line at the 180 Degree Location of the Hub.

The surface oil flow visualization of the $r/h=1.0$ radial hub and back wall in Figure 5-16(a) shows an overall lack of separated and reverse flow. The streamlines located within the diffuser shroud seem to wrap around the hub more on the left section of the image compared to the right, this matches the swirl direction induced by the upstream swirl vanes. However, once the shroud ends, the streamlines are accelerated radially towards the exit section of the collector

shown by the small arrows. A strong radial jet can be seen around the 0 degree location covering the upper portion of the hub, this is due to the exit flow from the shroud impinging on the hub and generating a vortex and separation line. A region of high secondary flow at the bottom portion of the hub is shown in Figure 5-16(b). Flow in this area is tightly confined between the exit of the diffuser, collector back wall and collector bottom. A separation line is shown due to the impingement on the hub generating counter-rotating pairwise vortices.

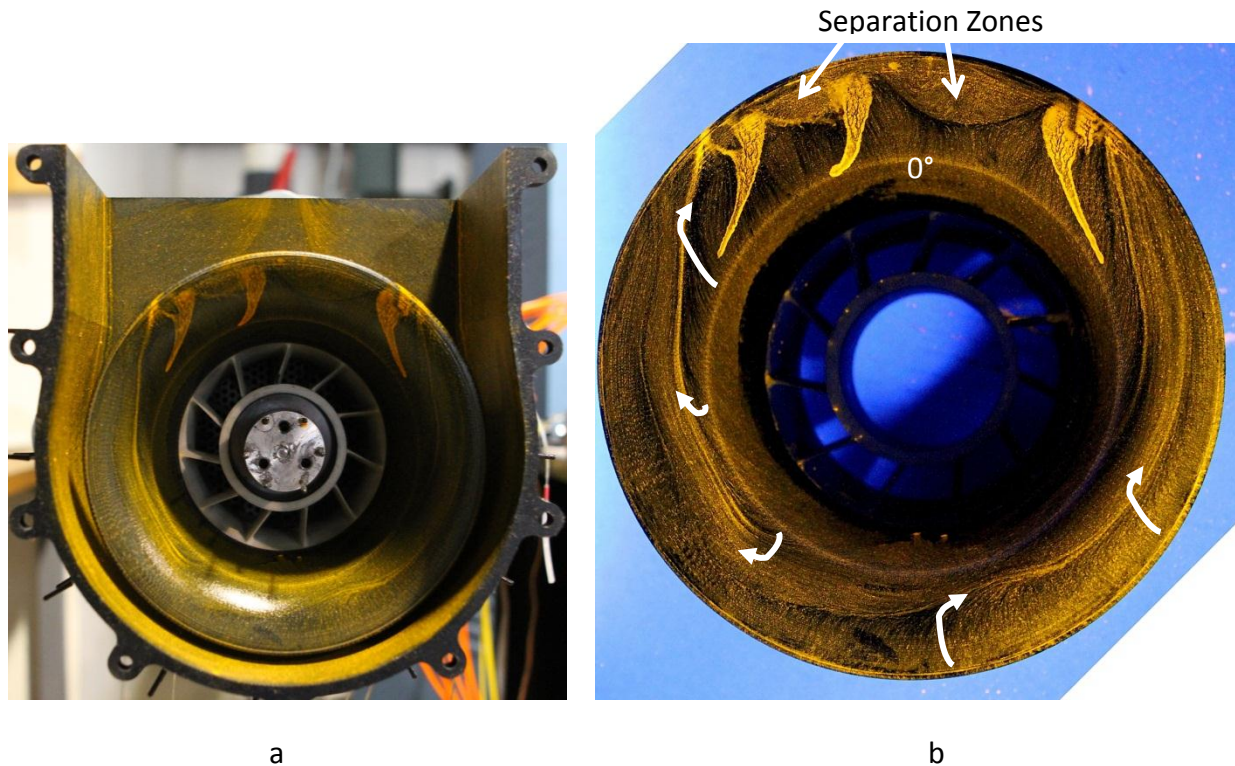


Figure 5-17: a) Experimental Setup of the $r/h=1.0$ Radial Diffuser Inside the Flat Wall ECB with the Back Wall and Hub Removed. b) Flow Separation Shown on the $r/h=1.0$ Radial Diffuser Shroud

The small gap between the bottom of the collector and exit of the $r/h=1.0$ radial diffuser is shown in Figure 5-17(a). The image was taken after the oil flow visualization was performed with the blower turned off; notice how the oil pools on the upper portion of the shroud begin to run due to gravity. Figure 5-17(b) above illustrates the highly separated flow on the $r/h=1.0$ radial diffuser shroud performed by a surface oil flow visualization. The flow exiting the diffuser was found to expand too rapidly, thus caused early flow separation around the majority of the diffuser. An area of reverse flow was found on the bottom section of the diffuser shroud due to the recirculation between the back wall and the bottom of the collector. The 0 degree location had large separation zones in which the flow detached from the diffuser shroud and rapidly exited the collector.

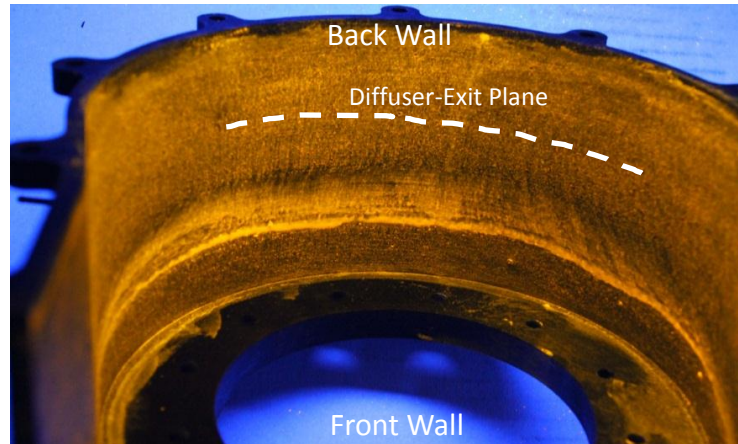


Figure 5-18: Surface Oil Flow Visualization of the Flat Wall Collector Using the $r/h=1.0$ Radial Hardware

The surface oil flow visualization shown in Figure 5-18 illustrates that the large radii of the $r/h=1.0$ diffuser effectively blocks the air flow traveling towards the front wall of the collector. A white curve has been drawn on the bottom of the collector representing the diffuser exit plane. The flow above the curve (close to the back wall) is washed around having difficult streamlines to trace verifying the existence of strong secondary flow in this region. The region below the curve or towards the front wall of the collector shows an area of stagnate oil representing the large diffuser radii creating a barrier between the diffuser exit and front wall. This barrier contributes to the high static pressure in the bottom region of the collector, thus limiting flow diffusion.

5.4 Cutback Radial Diffuser-Flat Wall Collector Analysis

A further optimized design was created by incorporating a combination of the $r/h=1.0$ and $r/h=0.25$ radial diffusers. This hybrid diffuser avoided areas of separated and reversed flow, allowing more uniform exit flow around the diffuser and into the collector box. Furthermore, this design allowed the flow to diffuse more efficiently by expanding to the front wall of the collector. The cutback radial diffuser was substituted in while using the existing $r/h=1.0$ radial hardware. Both Collectors were tested with the cutback radial diffuser and the flat wall collector outperformed the pinch.

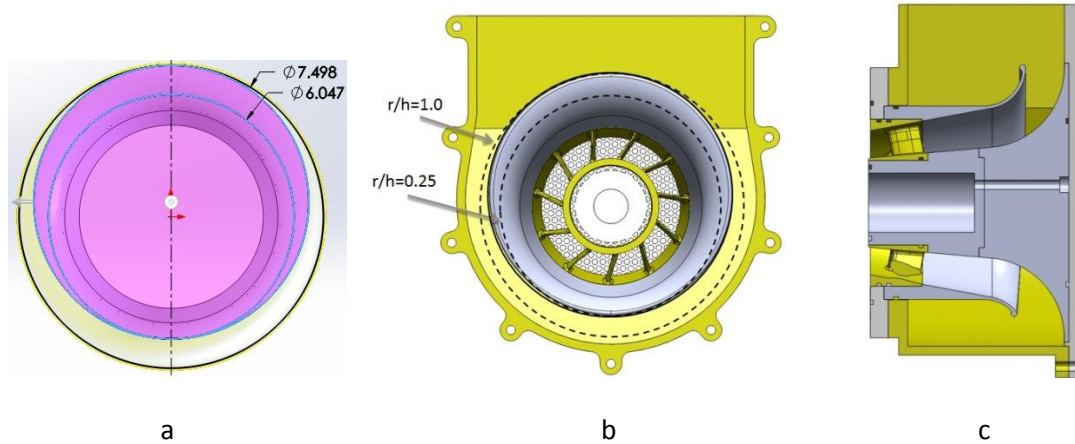


Figure 5-19: a) Cutback Radial Diffuser Design Shown in Solidworks. b) Radial Diffuser Comparison shown within the ECB c) Section View of the $r/h=0.25-1.0$ Cutback Radial Diffuser Inside of the Flat Wall Collector.

The design of this diffuser incorporated a circle with the radial height of the $r/h=1.0$ at the top and the height of the $r/h=0.25$ radii at the bottom. This new circle is shown in purple and the remaining yellow $r/h=1.0$ radial shroud surface area was cut away shown in Figure 5-19(a). The high secondary flow located in the bottom portion of the collector was reduced by opening the gap between the exit of the diffuser and the bottom of the collector. The distance between the diffuser exit and back wall was slightly increased at the 180 degree location by a quarter of an inch due to the smaller radii compared to the original $r/h=1.0$ diffuser.

5.4.1: Diffuser Inlet Parameters and Overall Subsystem Performance

The diffuser inlet results and overall subsystem performance variables for the $r/h=1.0$ radial diffuser incorporating the pinch collector and the cutback radial diffuser using the flat wall collector are shown below in Table 5-4.

Table 5-4: Performance Table Showing Experimental Inlet Run Conditions, Pressure Recoveries, and KEP Values. Comparing the r/h=1.0 Radial Diffuser with Pinch Collector to the Cutback Radial Diffuser with Flat Wall ECB. The Baseline Configuration is shown for Reference

	Baseline Diffuser-Collector	Pinch Collector w/ r/h=1.0 Radial Diffuser	Flat Wall Collector w/ r/h=0.25-1.0 Cutback Diffuser
Average Inlet Conditions			
Mach Number, Ma	0.397	0.399	0.408
Static Pressure	13.001	13.153	13.003
Static Δ Pressure	-0.593	-0.536	-0.796
Total Pressure	14.495	14.681	14.582
Total Δ Pressure	0.900	0.992	0.775
Dynamic Pressure	1.495	1.529	1.580
Swirl, α , deg	7.0	6.8	6.5
Overall Performance			
Pressure Recovery, C_p	39.7%	35.1%	50.7%
Diffuser Performance			
Diffuser Pressure Recovery	52.3%	52.9%	53.0%
Collector Performance			
KEP _y	3.25	4.84	3.12
KEP _{total}	5.23	6.56	4.41

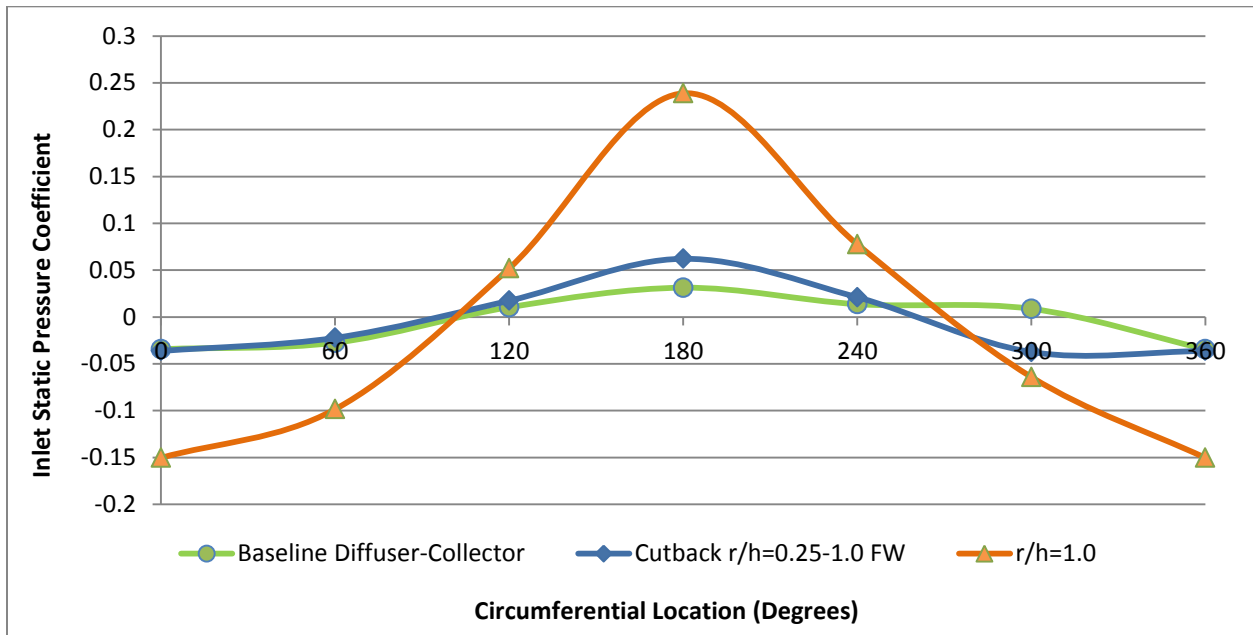


Figure 5-20: Circumferential Inlet Static Pressure Coefficient Distribution of r/h=1.0 radial diffuser and the Radial Cutback Design. Baseline Configuration is shown for Reference.

The cutback radial diffuser design kept the diffuser inlet static pressure distribution relatively uniform compared to the baseline and the original $r/h=1.0$ configurations as shown in Figure 5-20 above. The crucial feature to the cutback design is that it removed a large portion of the diffuser radii around the lower half of the shroud allowing airflow to effectively reach the front wall and diffuse within the ECB. The impact of the flat wall collector reduced the overall diffuser-collector subsystem pressure recovery by 2.3% compared to the cutback radial diffuser only test, providing a minimal negative impact on subsystem performance.

5.4.2: Collector Exit Section Data

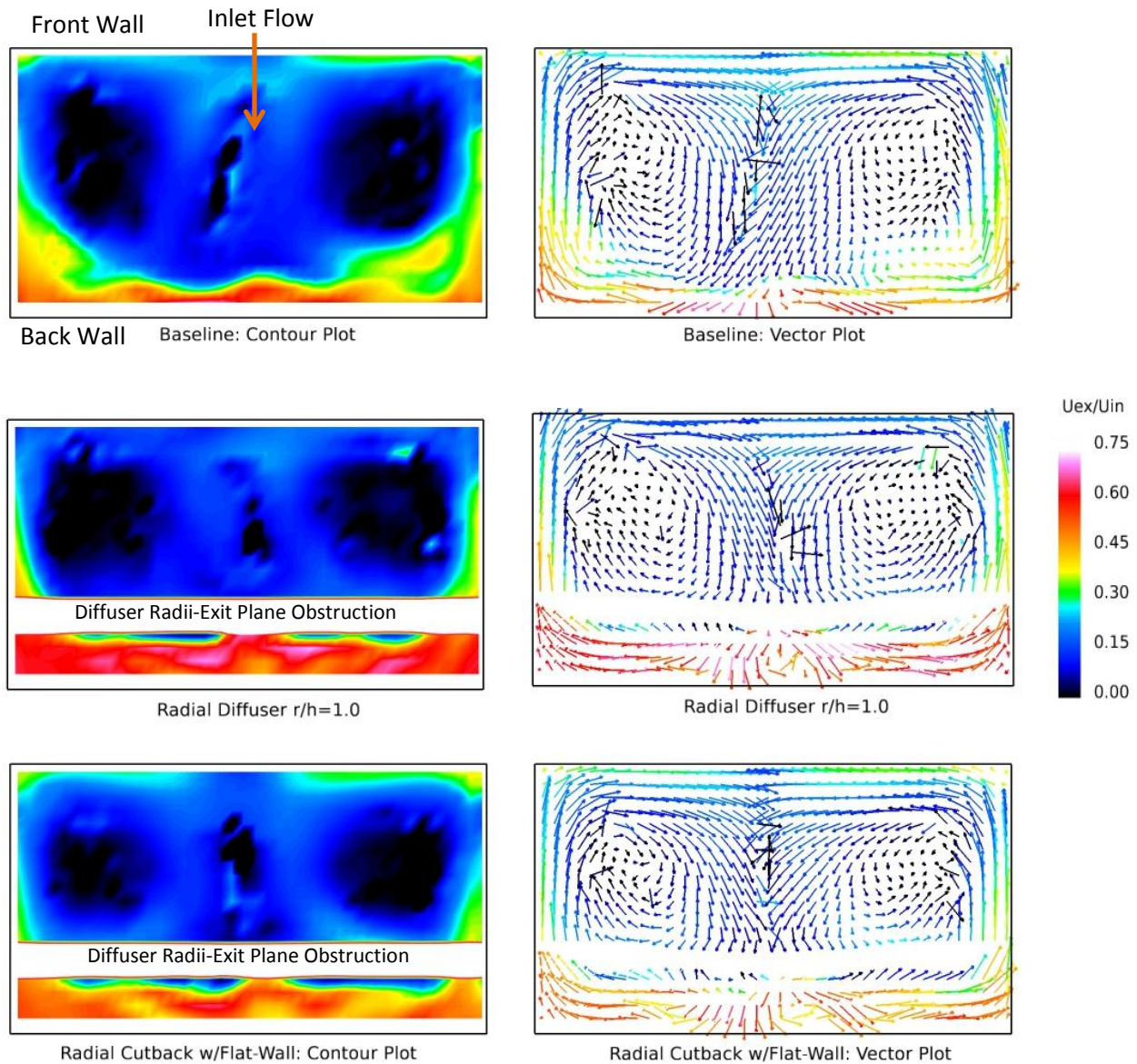


Figure 5-21: Contour and Vector Plot Comparison of the Baseline, $r/h=1.0$, and Cutback Radial Designs

The cutback diffuser incorporating the flat wall collector weakened the force of the impinging jet on the back wall compared to the original $r/h=1.0$ pinch collector design. The less red and white coloration in the contour plots in Figure 5-21 illustrates this impact. In effect, this weakened the recirculation zone off of the back wall, thus reduced the strength and size of the high loss cores creating a more uniform velocity outflow. The $r/h=0.25-1.0$ radial cutback design achieved beneficial lower KEP total values than both the baseline and original $r/h=1.0$ configurations by 0.82 and 2.15 respectively. Furthermore, the overall subsystem pressure recovery was improved from the baseline and $r/h=1.0$ configurations by 11% and 15.6% respectively.

5.4.3 Oil Flow Visualization

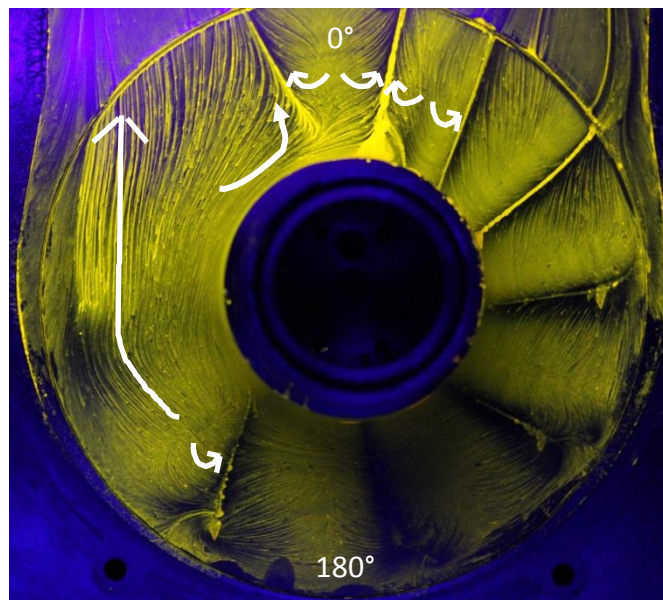


Figure 5-22: Oil Flow on the $r/h=1.0$ Radial Hub Incorporating the Cutback Radial Diffuser

The surface oil flow shows that the cutback radial diffuser design provided a more uniform diffuser outflow on the right side of the image shown by the numerous separation lines compared to the $r/h=1.0$. The separation lines are formed from a series of pairwise vortices from the diffuser outflow impinging on the hub, therefore more radial flow reached the hub with minimal reverse flow. The streamlines wrap around the hub on the left side of the image due to the same swirl factor as seen in the original $r/h=1.0$ design. This is a region of low momentum flow (shown by the long arrow) moving towards the exit section of the collector. A small region of upstream reverse flow is still noticeable on the top portion of the hub shown by the oil pool, but the flow downstream illustrates a great flow improvement.

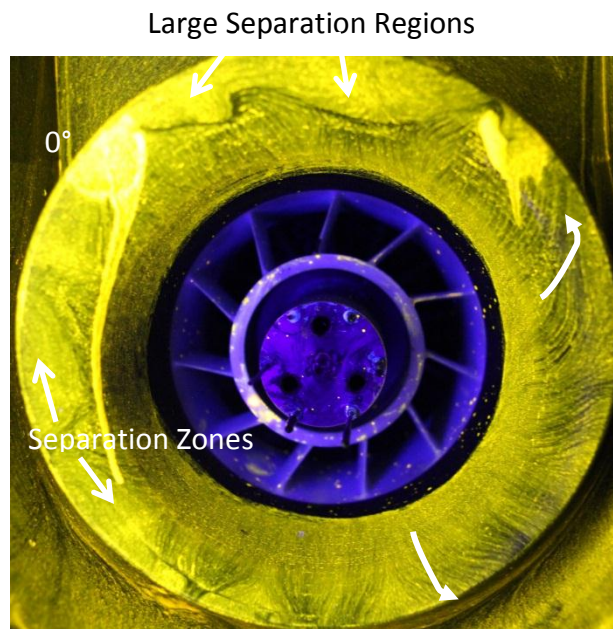


Figure 5-23: Oil Flow Visualization of the $r/h=0.25-1.0$ Cutback Radial Diffuser Shroud

The surface oil flow visualization on the upper portion of the cutback radial diffuser showed similar flow separation structures as on the original $r/h=1.0$ shroud due to minimal change in radii. The greatest performance benefit occurred at the lower portion of the diffuser shroud where the smaller radii produced a lower inlet static pressure, thus greatly reduced the effects of reverse flow on the diffuser wall. The secondary flow around the 180 degree location was reduced by cutting away part of the diffuser shroud and allowing the air to expand within the collector towards the front wall.

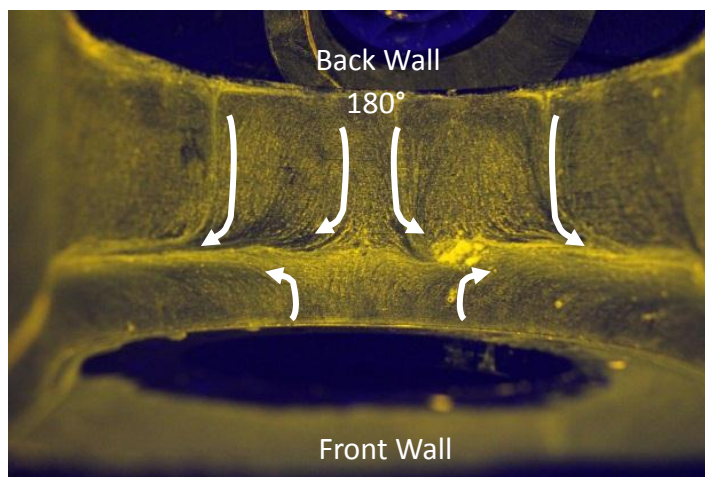


Figure 5-24: Flow in the Bottom Portion of the Flat Wall Collector Using the Radial $r/h=0.25-1.0$ Diffuser

The surface oil flow verified that by shortening the diffuser radius at the 180 degree location, flow was able to move back towards the front wall of the collector, thus promoted additional diffusion. The reverse flow on the bottom surface of the collector box split in the two different

directions due to the impingement on the back wall. The streamlines indicate that the flow traveled further toward the front wall due to the presence of low static pressure in this region compared to the higher static pressure found using the $r/h=1.0$ radial diffuser.

5.5: Diffuser Only Testing

In order to decipher the impact of the collector box on the overall subsystem pressure recovery, an experimental diffuser only test was performed. This test was run for the baseline diffuser and all of the radial diffuser designs including the cutback. For each diffuser of interest, a radial traverse was performed as explained in section 3.2 above, but without incorporating the collector box. The appropriate hub for each tested geometry was left installed to generate the correct flow path within the diffuser. A CAD section view along with the experimental diffuser only setup can be seen in the figures below.

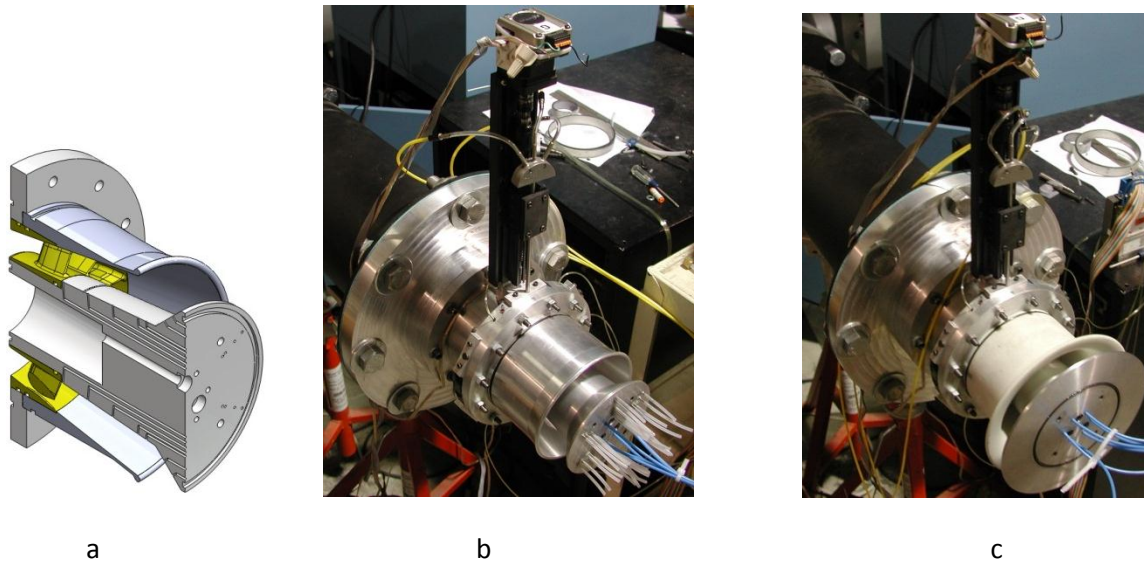


Figure 5-25: a) CAD Isometric Section View of the Baseline Diffuser Only Test. b) Experimental Setup of the Baseline Diffuser Test with Radial Traverse. c) Experimental Setup of the $r/h=1.0$ Radial Diffuser Hardware with Radial Traverse.

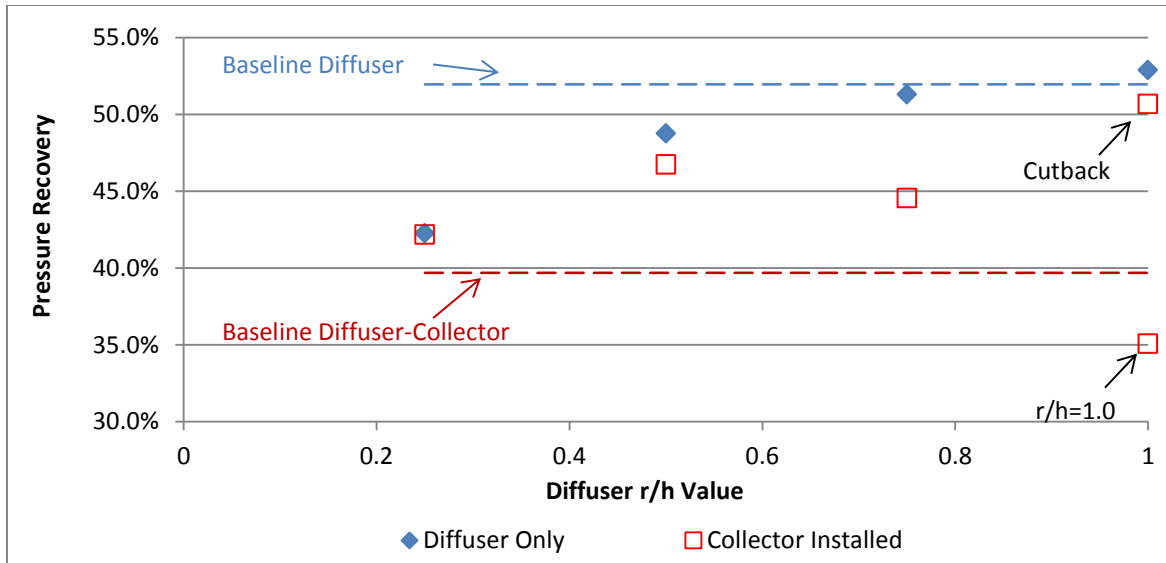


Figure 5-26: Plot of the Pressure Recovery versus the Diffuser r/h Value. Baseline Diffuser and Diffuser-Collector Lines added for comparison Purpose.

The pressure recovery vs. the diffuser r/h value plot above, illustrates the impact of the ECB on the overall subsystem pressure recovery. The blue diamonds represent the diffuser pressure recovery without the collector installed and the red squares represent the overall pressure recovery utilizing the pinch ECB or flat wall ECB for the cutback case. As the r/h value increases, the pressure recovery of the radial diffuser also increases shown by an almost near linear fit of the blue diamonds. The red Squares however show that the radial cutback diffuser performs the best within the overall subsystem given by the high diffuser only pressure recovery and low penalty of the collector. When combining the diffuser only and diffuser-collector trends of the pure radial diffusers, as the r/h value increases, the collector generates a more negative impact on the subsystem pressure recovery. This is shown by the increasing distance between the blue diamonds and red squares for a given r/h value. The dotted lines represent the baseline diffuser or diffuser-collector value for a means of reference.

6.1 Conclusion

A subsonic wind tunnel facility was designed and built to test and optimize a total of twenty different diffuser-collector geometry configurations at the one-twelfth scale. The facility provided the benefit of continuous operation with time-efficient accurate results incorporating interchangeable geometries. The custom built flow conditioning section located directly upstream of the diffuser-collector subsystem was effective in mimicking the exhaust flow from the last blade row of the LPT. Based on a 95% confidence interval, the inlet Mach number, Reynolds number, and overall subsystem pressure recovery were within an uncertainty of 1.74, 4.33, and 0.12 percent respectively.

Pressure measurements were taken using a 3-hole wedge probe traversed into the flow at the diffuser inlet, while a 5-hole “L” shaped probe was used at the collector exit. Multiple performance profile plots were generated from the pressure and total temperature data to provide insight of important flow features and reveal crucial areas for design improvements. A strong radial impingement was found on the back wall of the collector primarily due to the close proximity to the diffuser exit. Two large counter-rotating vortices were generated inside the exit section of the collector box restricting collector outflow and increasing the subsystem total pressure loss. Oil flow visualization was used to decipher the complex 3D flow occurring at the surface of particular diffuser-collector geometries to capture regions of detrimental separation and reverse flow.

Overall, the baseline diffuser-collector configuration was improved by over 10% in subsystem pressure recovery by implementing the cutback radial diffuser hardware and the flat wall collector box. The unique cutback radial diffuser design was able to recover the most amount of kinetic energy from the inlet of the diffuser while simultaneously kept the back pressuring effects relatively low. The design of the flat wall collector allowed airflow to dissipate back to the front wall and thus promote a more uniform cross sectional outflow compared to the baseline pinch design. The trade-off between an increased pressure recovery and minimal circumferential static pressure non-uniformity at the inlet of the diffuser (exhaust of the LPT) was reasonably met. The results show that the small scale diffuser-collector research facility serves as an advantageous bridge between conceptual design and full scale production all within a cost-effective manner.

6.2 Recommendations and Future Work

This research made confident that in order to achieve increased subsystem performance, the diffuser and collector must be designed as a system and not independently. Furthermore, it is to be noted that all of the interchangeable geometries used were to fit within the existing packaging restraints of the collector box. It is recommended that a parametric study be

performed to optimize the diffuser pressure recovery given a flat plate placed a certain axial distance from the diffuser exit. To keep everything within the existing collector restraints, by increasing the distance between the diffuser exit and flat plate, the axial length of the diffuser must be reduced. From here, the diffuser half angles could be modified as to provide the best expansion i.e. static pressure rise within the shortened distance without inducing early flow separation. This study would provide evidence as to the most efficient diffuser given the maximum axial distance increase from the flat plate. In general, the strength of the two detrimental counter-rotating vortices found within the exit section of the collector and back pressuring effects inside the diffuser could be greatly reduced possibly improving the overall subsystem performance even further.

Although over a 10% increase in overall subsystem pressure recovery was seen by use of the radial cutback design hardware, further geometry optimization is still possible to improve performance. The flow visualization shown on the cutback shroud identified large areas of separation around the 0 degree location. These areas decrease the performance potential of the diffuser by lowering the amount of available static pressure rise. It's possible that these areas could be improved by changing the shroud to exit at an angle smaller than 90 degrees. By reducing the shroud exit angle, flow is more likely to stay attached to the walls, thus promote additional expansion instead of early separation.

The one-twelfth scale cutback radial diffuser hardware using the flat wall collector will be experimentally evaluated in the one-quarter scale facility in the near future. At the one-twelfth scale, the inlet Reynolds number based on hydraulic diameter is an order of magnitude smaller than the quarter and full scale production models. For the same geometry, it was found that the overall subsystem pressure recovery was also smaller compared to the quarter and full scale. It is reasonable to believe the static pressure coefficient will be nearly independent of Reynolds number for $U_1 \Delta R_1 / \nu > 7 \times 10^4$ [(Blevins, 1984)]. This statement is valid when applied to an annular diffuser with moderate swirl and free discharge. By having incompressible flow from a radial diffuser impinge on a flat plate, the static pressure recovery will be nearly independent of Reynolds number for $R_d > 2 \times 10^5$. For Reynolds numbers below this value, the pressure recovery drops off rapidly [(Moller, 1966)]. The one-twelfth scale facility operated with Reynolds numbers slightly above this value. Further insight will be gathered as to the effect of the overall subsystem pressure recovery due to the change in inlet Reynolds number. The experimental validity test between the two scaled diffuser-collector facilities will be performed utilizing the same cutback subsystem configuration.

References

- Aeroprobe Corp. (2006). *Multi-Hole Probe User's Manual for 5-Hole and 7-Hole Probes* (Vol. 1.21). Blacksburg, VA.
- Bernier, B. C., Kapat, J. S., & Ricklick, M. (2011). *Impact of a Collector Box on the Pressure Recovery of an Exhaust Diffuser System*. University of Central Florida. ASME Turbo Expo GT2011-46455.
- Blevins, R. D. (1984). *Applied Fluid Dynamics Handbook*. Van Nostrand Reinhold Co.
- Busch Inc. (n.d.). *Busch Panther WA 3032-3300D*. Retrieved from Rotary Lobe, Positive Displacement Blower:
http://www.buschusa.com/fileadmin/Companies/USA/PDFs/Panther/Panther_WA.pdf
- Camci, C., & Rizzo, D. H. (2001). *Secondary Flow and Forced Convection Heat Transfer Near Endwall Boundary Layer Fences in a 90° Turning Duct*. The Pennsylvania State University. *International Journal of Heat and Mass Transfer* 45. Elsevier Science Ltd.
- Hardin, J. R. (2010, June 8). *Patent No. US 7,731,475 B2*. United States.
- Hoffmann, J. A. (1981). *Effects of Free-Stream Turbulence on Diffuser Performance*. California Polytechnic State University. San Luis Obispo: *Journal of Fluids Engineering*. ASME.
- Hunt, J., Abell, C. J., Peterka, J. A., & Woo, H. (1978). *Kinematical Studies of the Flows Around Free or Surface-Mounted Obstacles; Applying Topology to Flow Visualization*. *Journal of Fluid Mechanics*.
- Moller, P. S. (1966). *A Radial Diffuser Using Incompressible Flow Between Narrowly Spaced Disks*. University of California Davis. *Journal of Basic Engineering*. ASME.
- Nanda, D. D., Pruthi, R., & Ansari, A. I. (2012, February 9). *Patent No. US 2012/0034064 A1*. United States.
- Omega. (n.d.). *Temperature-to-Analog Converter Battery or AC Powered*. Retrieved from Omega TAC80B-K Thermocouple Spec Sheet:
<http://www.omega.com/Temperature/pdf/TAC80B.pdf>
- Roach, P. E. (1987). *The generation of Nearly Isotropic Turbulence by Means of Grids*. Rolls Royce Ltd. *International Journal of Heat and Fluid Flow*.

- Samal, N. R. (2011). *Design of a Subsonic Wind Tunnel Facility for the Evaluation of a Diffuser-Collector Subsystem Using Stereo PIV*. Blacksburg: Virginia Polytechnic Institute and State University.
- Scanivalve Corp. (2005, November). *ZOC 17 Electric Pressure and Scanning Module*. Retrieved from Instruction and Service Manual:
<http://www.scanivalve.com/services/downloadfile.ashx?file=/media/4284/zoc17man.pdf>
- Solid Concepts Inc. (2009, January). *SLS Polyamide Properties*. Retrieved from
http://www.solidconcepts.com/content/pdfs/literature/SLS_Brochure.pdf
- Solid Concepts Inc. (2010, June). *Stereolithography Material Properties*. Retrieved from
http://www.solidconcepts.com/content/pdfs/literature/SLA_PolyJet_Brochure.pdf
- Sovran, G., & Klomp, E. D. (1967). *Experimentally Determined Optimum Geometries for Rectilinear Diffusers with Rectangular, Conical or Annular Cross-Section*. Fluid Mechanics of Internal Flow. Elsevier Publishing Co.
- Sudo, K., Sumida, M., & Hibara, H. (1998). *Experimental Investigation on Turbulent Flow in a Circular-Sectioned 90-Degree Bend*. Experiments in Fluids 25. Springer-Verlag.
- Sudo, K., Sumida, M., & Hibara, H. (2001). *Experimental Investigation on Turbulent Flow in a Square-Sectioned 90-Degree Bend*. Experiments in Fluids 30. Springer-Verlag.
- Takamura, T. (1983, July 5). *Patent No. 4,391,566*. United States.
- United Sensor Corp. (2011). *2-Dimensional Probe Standard Specifications*. Retrieved from Three-hole Wedge Shaped: <http://www.unitedsensorcorp.com/2d-specs.html>
- Vassiliev, V., Rothbrust, M., & Irmisch, S. (2008). *Refitting of Exhaust Diffuser of Industrial Gas Turbine*. ALSTOM. ASME Turbo Expo. GT2008-50165.
- Zhu, X., Wang, H., & Du, Z. (2010). *Aerodynamic Optimization for a Low Pressure Turbine Exhaust Hood Using Kriging Surrogate Model*. Shanghai Jiao Tong University. International Communications in Heat and Mass Transfer. Elsevier Ltd.

Radial Hub Geometry and Results

In addition to the baseline, titled diffuser, and radial diffuser components mentioned above, a radial hub geometry was also designed and experimentally tested. The hub was manufactured out of aluminum 6061 material and was made to properly mate with the existing smaller diameter hub section and the baseline back wall. Unlike the baseline hub, the radial hub was not designed with inner tunnels for pressure taps as only the impact of the outer geometry on the overall subsystem pressure recovery was of interest.

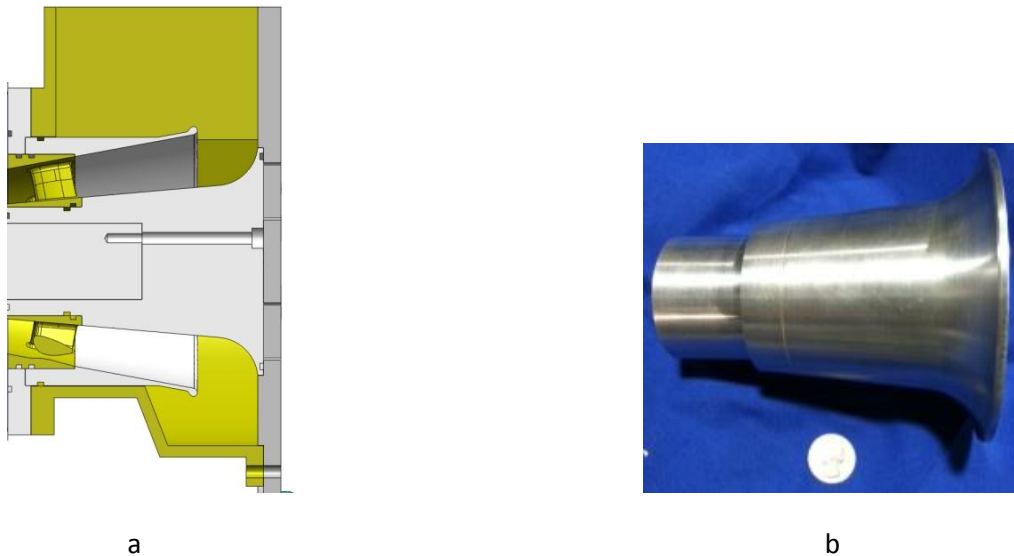


Figure A-1: Section View of the Radial Hub Geometry Using the Baseline Components. b) Experimental Radial Hub Shown to Scale by a Quarter.

Table A-1: Radial Hub Design Performance Table Showing Experimental Inlet Run Conditions, Pressure Recoveries, and KEP Values.

	Baseline Diffuser-Collector	Pinch Collector w/Radial Hub	Flat-Wall Collector w/Radial Hub
<u>Average Inlet Conditions</u>			
Mach Number, Ma	0.397	0.397	0.398
Static Pressure	13.001	13.052	13.058
Static Δ Pressure	-0.593	-0.551	-0.546
Total Pressure	14.495	14.553	14.566
Total Δ Pressure	0.900	0.949	0.965
Dynamic Pressure	1.495	1.501	1.508
Swirl, α , deg	7.0	6.4	6.7
<u>Overall Performance</u>			
Pressure Recovery, Cp	39.7%	36.7%	36.1%
<u>Diffuser Performance</u>			
Diffuser Pressure Recovery	52.3%	NA	NA
<u>Collector Performance</u>			
KEP_y	3.25	INC	3.73
KEP_total	5.23	INC	5.93

As shown from the performance summary table above, both the pinch and flat-wall collector box geometries were experimentally tested and analyzed. The baseline diffuser and back wall components were used for each case. The results show that for both collectors, the overall subsystem pressure recovery is less than the baseline model by at least 3% when using the radial hub. Furthermore, an exit traverse using the flat-wall ECB was performed and the both the KEP_y and KEP_total values were confirmed to be higher than the baseline. In conclusion, the radial hub hardware yielded no performance benefit compared to the baseline model and was therefore considered of no interest.

[Acura 60 Struts and Swirl Vanes](#)

The original struts and swirl vanes were made from a material called Acura 60 premium Stereolithography Rapid Prototyping (SLA). This material provided a smoother surface and sharper, less thick walls having a minimum wall thickness of 0.020 inches compared to the SLS material of 0.030 inches. Although more detail was provided given the SLA material, its heat deflection property was set at only 120 degrees Fahrenheit. Therefore, when using the blower under normal operating testing conditions of at least 130 degrees Fahrenheit, the SLA heat deflection value was exceeded and deformation of the struts and swirl vanes were seen. The deformation proved detrimental to the swirl vanes due to its thin walled airfoils causing detachment from the main ring. The SLA struts and swirl vanes were removed and substituted with a higher temperature deflection material of near 350 degrees Fahrenheit using SLS.



Figure A-2: A Side by Side Comparison of the SLA material Strut Ring Shown in Black and the SLS Material Strut Ring Shown in White. O-rings are Included on the SLS Version.

Appendix B – Additional Testing and Trends

Turning Strut Ring 180 Degrees

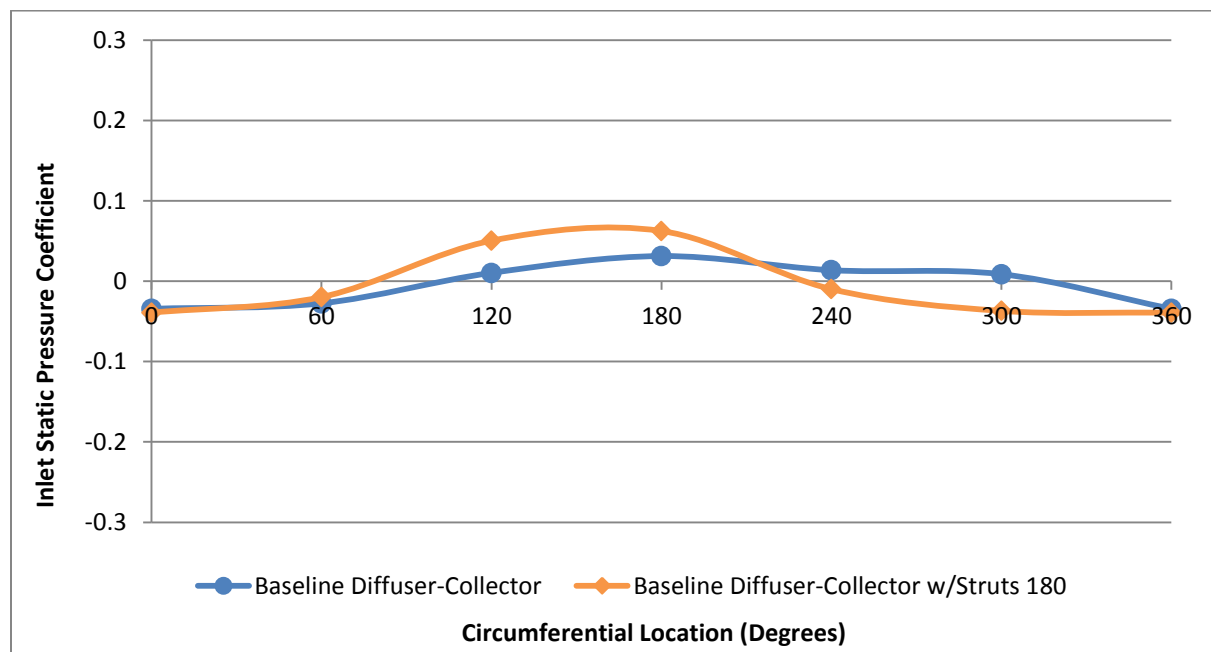


Figure B-1: Comparison of the Circumferential Static Pressure Distribution with the Strut Ring Turned 180 Degrees

The specific clocking of the strut ring played an important role in the inlet static pressure coefficient circumferential distribution. An experiment was setup in which the strut ring was turned 180 degrees from its original clocking and a full radial traverse was performed. The result shown in figure B-1 illustrates that the inlet static pressure coefficient changed (orange)

compared to the original clocking (blue). After further investigation it was discovered by use of the CMM that the strut ring was off by approximately eleven thousandths of an inch, thus verifying nonconcentric circles. This offset was considered satisfactory through the manufacture by providing fifteen thousandths of an inch tolerance on all its SLS glass-filled nylon 12 parts. To account for this slight offset, all geometries were run using the same strut ring clocking.

Calculation of Subsystem Pressure Recovery Based on a Trendline

For each geometry configuration, both the flat-wall and the pinch collector were installed as shown in Appendix C. By testing both collectors, the impact of the collector geometry on overall subsystem performance could be studied. Inlet data was taken from the circumferential hub and case pressure taps with no probe inserted in the flow. Using the differential pressure between the raw measured value and the atmospheric pressure for each pressure tap location, a total of 12 differential pressures were calculated. The average of these 12 values was taken representing a “snap shot” of the diffuser inlet static pressure profile. As more detailed experimental data was acquired through the use of the radial traverse, a plot was created of the overall pressure recovery of the system versus the average inlet differential pressure value.

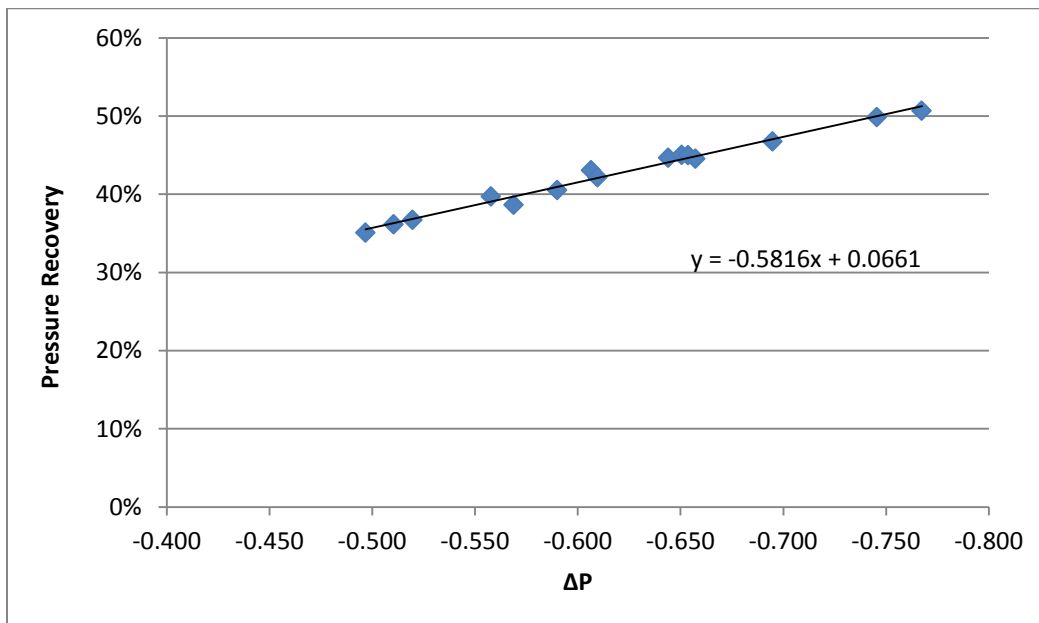


Figure B-2: Plot of overall subsystem pressure recovery calculated from radial traverse measurements vs. average differential pressure at the diffuser inlet. The Trendline and Equation are shown.

By plotting the experimental data as shown above, a trend line can be calculated representing the best fit through the data points. Using the equation of the trend line, an estimated overall subsystem pressure recovery can be found given any diffuser-collector average inlet differential pressure value. This pressure recovery-trendline technique was found very useful in accurately predicting the pressure recovery of the system within an average 1% error without having to perform a full circumferential radial traverse for each collector box geometry, saving time and effort.

Appendix C – All Experimentally Tested Diffuser-Collector Configurations



Performance optimization of a subsonic Diffuser-Collector subsystem using interchangeable geometries

For any additional documentation related to this thesis, please contact Brian P. Boehm.

Email: bboehm@vt.edu

Copyright 2012, Brian P. Boehm